iScience

CellPress
OPEN ACCESS

Article

Coproduction of hydrogen and lactic acid from glucose photocatalysis on band-engineered $Zn_{1-x}Cd_xS$ homojunction

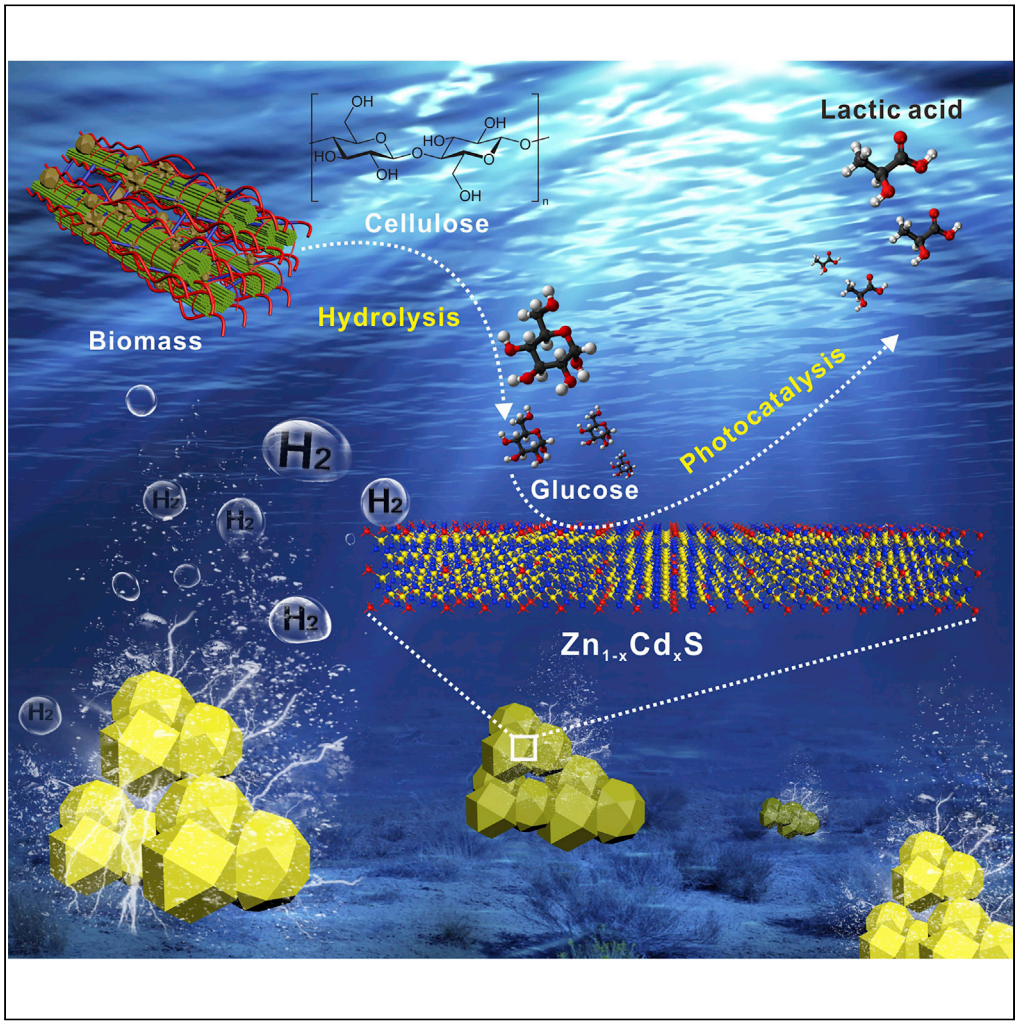

Heng Zhao, Chao-Fan Li, Xue Yong, ..., Zhangxin Chen, Md Golam Kibria, Jinguang Hu

zhiyi.hu@whut.edu.cn (Z.-Y.H.)
md.kibria@ucalgary.ca (M.G.K.)
jinguang.hu@ucalgary.ca (J.H.)

HIGHLIGHTS

$Zn_{1-x}Cd_xS$ ZB-WZ homojunction was designed to improve charge separation efficiency

Bandgap engineering improved the hydrogen production from glucose photoreforming

Optimized $Zn_{0.6}Cd_{0.4}S$ ZB-WZ exhibited high lactic acid yield and selectivity

Rational photocatalyst design realizes biomass valorization and H_2 coproduction

Zhao et al., iScience 24, 102109
February 19, 2021
https://doi.org/10.1016/j.isci.2021.102109

iScience

CellPress
OPEN ACCESS

Article

Coproduction of hydrogen and lactic acid from glucose photocatalysis on band-engineered $Zn_{1-x}Cd_xS$ homojunction

Heng Zhao,[1] Chao-Fan Li,[2,3] Xue Yong,[4] Pawan Kumar,[1] Bruna Palma,[1] Zhi-Yi Hu,[2,3,*] Gustaaf Van Tendeloo,[3,5] Samira Siahrostami,[4] Stephen Larter,[6] Dewen Zheng,[7] Shanyu Wang,[7] Zhangxin Chen,[1] Md Golam Kibria,[1,*] and Jinguang Hu[1,8,*]

SUMMARY

Photocatalytic transformation of biomass into value-added chemicals coupled with co-production of hydrogen provides an explicit route to trap sunlight into the chemical bonds. Here, we demonstrate a rational design of $Zn_{1-x}Cd_xS$ solid solution homojunction photocatalyst with a pseudo-periodic cubic zinc blende (ZB) and hexagonal wurtzite (WZ) structure for efficient glucose conversion to simultaneously produce hydrogen and lactic acid. The optimized $Zn_{0.6}Cd_{0.4}S$ catalyst consists of a twinning superlattice, has a tuned bandgap, and displays excellent efficiency with respect to hydrogen generation (690 ± 27.6 $\mu mol \cdot h^{-1} \cdot g_{cat.}^{-1}$), glucose conversion (~90%), and lactic acid selectivity (~87%) without any co-catalyst under visible light irradiation. The periodic WZ/ZB phase in twinning superlattice facilitates better charge separation, while superoxide radical ($\cdot O_2^-$) and photogenerated holes drive the glucose transformation and water oxidation reactions, respectively. This work demonstrates that rational photocatalyst design could realize an efficient and concomitant production of hydrogen and value-added chemicals from glucose photocatalysis.

INTRODUCTION

There has been growing interest in developing a "biorefinery" platform as opposed to the century-old petroleum refinery analogous for sustainable production of fuels and chemicals (Ragauskas, et al., 2006) Unfortunately, two technologically advanced biorefinery platforms, including the thermochemical processes (such as combustion, pyrolysis, and gasification) and biological processes (such as enzymatic hydrolysis and micro-organisms fermentation) are facing setbacks due to carbon-intensive and expensive processes involved therein (Huber, et al., 2006; Rubin, 2008). Among other emerging routes, solar-driven biomass photocatalysis (the so-called photo-biorefinery) is appealing to realize solar energy storage into chemical bonds with high energy density(Butburee, et al., 2020; Zhao, et al., 2021; Wu et al., 2020a, 2020b; Wu, et al., 2017; Zhang et al., 2017a, 2017b). As one of the most abundant biomass-based compounds, glucose has been utilized to produce various value-added chemicals like glucaric acid, gluconic acid, 5-hydroxymethylfurfural, and lactic acid(Liu et al., 2020a, 2020b; Zhang and Huber, 2018). Lactic acid, a natural organic acid with extremely wide applications in food, chemical, and pharmaceutical fields, could be used as a monomer to produce biodegradable polylactic acid for medical, packaging, electronic applications (Komesu, et al., 2017). Lactic acid has been regarded as one of the most important hydroxycarboxylic acids, and its global market in 2020 is projected to reach USD 3.82 billion with a compound annual growth rate of 18.6%. Currently, lactic acid is mainly produced by microorganisms and chemical synthesis. Microorganism fermentation could reduce the cost of lactic acid production while chemical synthesis could improve the quality of lactic acid. However, the tedious and expensive procedures involved in these two approaches stimulate the exploration for novel and facile methods to produce lactic acid (Maki-Arvela, et al., 2014).

Photocatalytic glucose conversion to selectively generate lactic acid by rationally designing catalysts and reaction conditions is appealing as the photo-generated electrons could also reduce proton to hydrogen simultaneously (Wu et al., 2020a, 2020b). Photocatalytic water splitting suffers from a low quantum efficiency due to the slow kinetics of the redox reactions and high recombination of photogenerated electrons

[1]Department of Chemical and Petroleum Engineering, University of Calgary, 2500 University Drive, NW, Calgary, Alberta T2N 1N4, Canada

[2]State Key Laboratory of Advanced Technology for Materials Synthesis and Processing, Wuhan University of Technology, 122 Luoshi Road, Wuhan, Hubei 430070, China

[3]Nanostructure Research Centre (NRC), Wuhan University of Technology, 122 Luoshi Road, Wuhan, Hubei 430070, China

[4]Department of Chemistry, University of Calgary, Calgary, Alberta T2N 1N4, Canada

[5]Electron Microscopy for Materials Science (EMAT), University of Antwerp, 171Groenenborgerlaan, B-2020 Antwerp, Belgium

[6]Department of Geosciences, University of Calgary, 2500 University Drive, NW, Calgary, Alberta T2N 1N4, Canada

[7]Research Institute of Petroleum Exploration and Development (RIPED), CNPC, Beijing 100083, China

[8]Lead Contact

*Correspondence: zhiyi.hu@whut.edu.cn (Z.-Y.H.), md.kibria@ucalgary.ca (M.G.K.), jinguang.hu@ucalgary.ca (J.H.)

https://doi.org/10.1016/j.isci.2021.102109

and holes. Herein, excess sacrificial reagents are often needed as electron donors/acceptors to timely consume the photo-generated holes/electrons (Schneider and Bahnemann, 2013). This is apparently not sustainable as these sacrificial reagents are expensive and often toxic. Alternatively, glucose with abundant hydroxyl groups could act as an electron donor to react with photo-generated holes during the photocatalytic reaction (Jin, et al., 2017; Iervolino, et al., 2017; Nguyen, et al., 2019). However, over-oxidation of glucose always leads to CO_2 production which compromises the photo-efficiency and increases the net cost. Therefore, rational catalyst design to selectively convert glucose to value-added products with minimal CO_2 production along with hydrogen production is absolutely a promising research direction.

Efficient charge separation and proper redox potential are the two key factors for designing catalysts for glucose photocatalysis to simultaneously produce hydrogen and useful organics such as lactic acid. To realize this concept, coupling two different semiconductor photocatalysts to form a heterojunction has been demonstrated as a feasible approach owing to the improved interfacial charge transfer and facile bandgap regulation (Mayer, et al., 2013; Duan, et al., 2020). However, limited by substantial charge carrier loss at the mismatched lattice interfaces in the heterojunction and the disordered distribution of the heterojunction within these composites, it would be speculative to solely ascribe the difference in photocatalytic performance to the heterojunctions. Besides, due to the randomness of the heterojunction formation, it would be difficult to precisely tailor the distribution and content. Alternatively, a homojunction constructed by a twinning superlattice (TSL) in nanocrystals stands out in terms of its efficient charge separation for photocatalyst design with the II-VI and III-V group semiconductors (Algra, et al., 2008; Liu, et al., 2013; Jin, et al., 2020). Considering the redox potential regulation, bandgap engineering should be also combined with homojunction to improve the product selectivity from glucose photocatalysis (Chaves, et al., 2020; Ning, et al., 2017). To realize these concepts in rational photocatalyst design, solid solution, an alloy phase in which solute atoms are dissolved in the solvent lattice while still maintaining the solvent type, shows significant advantages compared with other approaches like quantum size effect and doping in terms of preparation procedure and uniformity (Holmes, et al., 2012; Asahi, et al., 2014; Choi, et al., 1994).

Herein, we report the development of a visible-light-driven $Zn_{1-x}Cd_xS$ solid solution photocatalyst to simultaneously produce hydrogen and lactic acid from glucose photoreforming via introducing zinc blende (ZB)-wurtzite (WZ) TSL homojunction structure and fine regulating bandgap structure. The optimized photocatalyst achieved high efficiency for hydrogen evolution (690 ± 27.6 $\mu mol \cdot h^{-1} \cdot g_{cat.}^{-1}$) and glucose conversion (~90%) with high selectivity (~87%) of lactic acid generation. Subsequently, we extended the substrates to other monosaccharides, disaccharide (cellobiose), and polysaccharide (Avicel) with a more complicated molecular structure to demonstrate the concomitant production of lactic acid and hydrogen. This present work could shed new light on the efficient utilization of saccharides or even biomass to produce sustainable hydrogen fuel and high value-added products by a rational design of photocatalysts.

RESULTS AND DISCUSSION

Catalyst design

Cubic ZB and hexagonal WZ crystals both exist naturally in II-VI and III-V group semiconductors. The atomic stacking sequence of ZB is A-B-C-A-B-C while the WZ endows the A-B-A-B stacking sequence (Ricolleau, et al., 1999). As these two crystal structures have almost the same lattice constants, a homojunction structure by bridging ZB and WZ segments usually occurs with long-range order, resulting in a TSL (Figure 1A) (Zhang et al., 2017a, 2017b). The formed homojunction structure has been widely reported to improve the photocatalytic activity by enhancing the charge separation efficiency, as the photogenerated electrons and holes would spontaneously migrate into ZB and WZ segments respectively (Figure 1B) (Pemasiri, et al., 2009; Jacopin, et al., 2011; Zhang et al., 2017a, 2017b). More importantly, accompanied by changing the ratio of Zn:Cd, $Zn_{1-x}Cd_xS$ solid solutions will have different bandgap structures (Figure 1C), as evidenced by UV-vis absorbance spectra (Figure S1). Along with increasing the ratio of Zn:Cd in the TSL, the catalyst will have a large bandgap with enhanced reduction and oxidation potential for hydrogen production and glucose conversion, respectively, while sacrificing visible light absorbance. Herein, we designed and fabricated $Zn_{1-x}Cd_xS$ solid solutions with ZB-WZ homojunction structure to improve the charge separation efficiency, thus realizing enhanced hydrogen and lactic acid production from glucose photocatalysis.

Catalyst characterizations

The detailed ZB-WZ TSL with a homojunction structure of $Zn_{1-x}Cd_xS$ solid solutions, obtained by atomic substitution rather than simply physical mixing, has been investigated by scanning electron microscopy

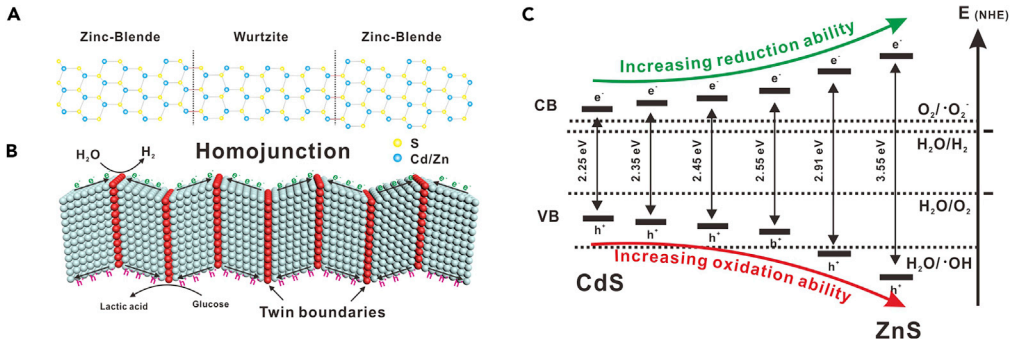

Figure 1. Schematic illustration of homojunction and bandgap structures of $Zn_{1-x}Cd_xS$ solid solutions

(A) Schematic atomic model of a zinc blende (ZB)-wurtzite (WZ) superlattice structure.

(B) Twin boundaries in homojunction and the migration of charge carriers.

(C) Bandgap structure of $Zn_{1-x}Cd_xS$ solid solutions.

and transmission electron microscopy (TEM) analysis. All the $Zn_{1-x}Cd_xS$ solid solutions exhibit a distinct nanoparticle morphology with a clean surface in field emission scanning electron microscope (FE-SEM) images (Figures S2 and S3). The selected area electron diffraction (SAED) patterns over a large area (Figure 2C) show that the WZ phase and ZB phase co-exist in the sample. However, SAED patterns are obtained over regions as large as a few hundred nanometer and are unable to present local structural information of the nanoparticles. Therefore, high-resolution high-angle annular dark-field scanning transmission electron microscopy (HR-HAADF-STEM) has been performed. The results demonstrate that two different nanoparticles (Figures 2A and 2B upper insets) are WZ phase, imaged along the [11-23] zone axis (Figure 2A), and ZB, imaged along [110] zone axis (Figure 2B), respectively. The energy dispersive X-ray spectroscopy (EDS) elemental maps at low magnification (Figure S4) indicate that the Cd, Zn, and S are uniformly distributed on every nanoparticle. Even on the atomic-scale EDS elemental maps (Figures 2D–2F), the Cd and Zn atoms are homogeneously distributed in every atomic column which corresponds to the character of a solid solution (Ding, et al., 2019). Meanwhile, the S atomic column and Cd/Zn atomic column can be distinguished by atomic resolution high-angle annular dark-field scanning transmission electron microscopy (HAADF-STEM) (Figure 2G), which are drift corrected using the RevSTEM program (Sang and LeBeau, 2014). The S atomic columns show up as darker dots, while the Cd/Zn atomic columns are the brighter dots (indicated by arrows). It is caused by the fact that the HAADF-STEM contrast is roughly proportional to the atomic number squared (S being much lighter than Cd/Zn), which is the so-called "Z-contrast"(Pennycook and Jesson, 1991). The Cd/Zn ratio of per Cd/Zn atomic column can be estimated by quantitative scanning transmission electron microscopy (STEM) based on the intensities of the scattering electrons (Klenov and Stemmer, 2006; Van Aert, et al., 2009). Hence, the positions and normalized scattered intensity of each Cd/Zn atomic column are presented via the StatSTEM program (Figure 2H) (De Backer, et al., 2016). The intensity of each Cd/Zn atomic column is proportional to the average atomic weight, which is directly related to the Cd/Zn ratio of per column. The higher normalized scattered intensities (histogram in Figure 2H) indicate Cd/Zn columns having more Cd atoms. Although the global Cd/Zn ratio (0.4:0.6) is maintained, slight differences of the local Cd/Zn distribution can be revealed at the atomic scale. Another notable fact is the presence of a large amount of twin boundaries with inversion symmetry in the ZB nanoparticles (Figures 2B and S5A). These twin boundaries can also be regarded as a thin WZ phase layer (Figure S5B). Hence, these twin boundaries with inversion symmetry construct a kind of ZB-WZ-ZB layered homojunction, which could improve the separation of excited electrons and holes (Liu, et al., 2013). In summary, atomic-resolution STEM analysis has established a homogeneous distributed $Zn_{1-x}Cd_xS$ solid solution with two different phases (WZ and ZB). The twin boundaries within the ZB nanoparticles establish twin-induced ZB-WZ-ZB homojunctions.

Also, X-ray diffraction (XRD) reveals the presence of ZB-WZ TSL in all the $Zn_{1-x}Cd_xS$ samples (Figure S6). The as-prepared CdS showed typical WZ crystal phase with low content of ZB while ZnS mainly exhibited ZB crystal phase with low concentration of WZ (Figure S7). Besides, the as-fabricated CdS shows an unusual diffraction intensity of the (002) facet in comparison with the reference pattern, indicating that a large number of (002) facets are exposed in our photocatalysts. Due to the smaller radius of Zn^{2+} (0.74 Å), the XRD peak positions continuously shift to a higher angle when substituting some Cd^{2+} (0.97 Å) with Zn^{2+} and

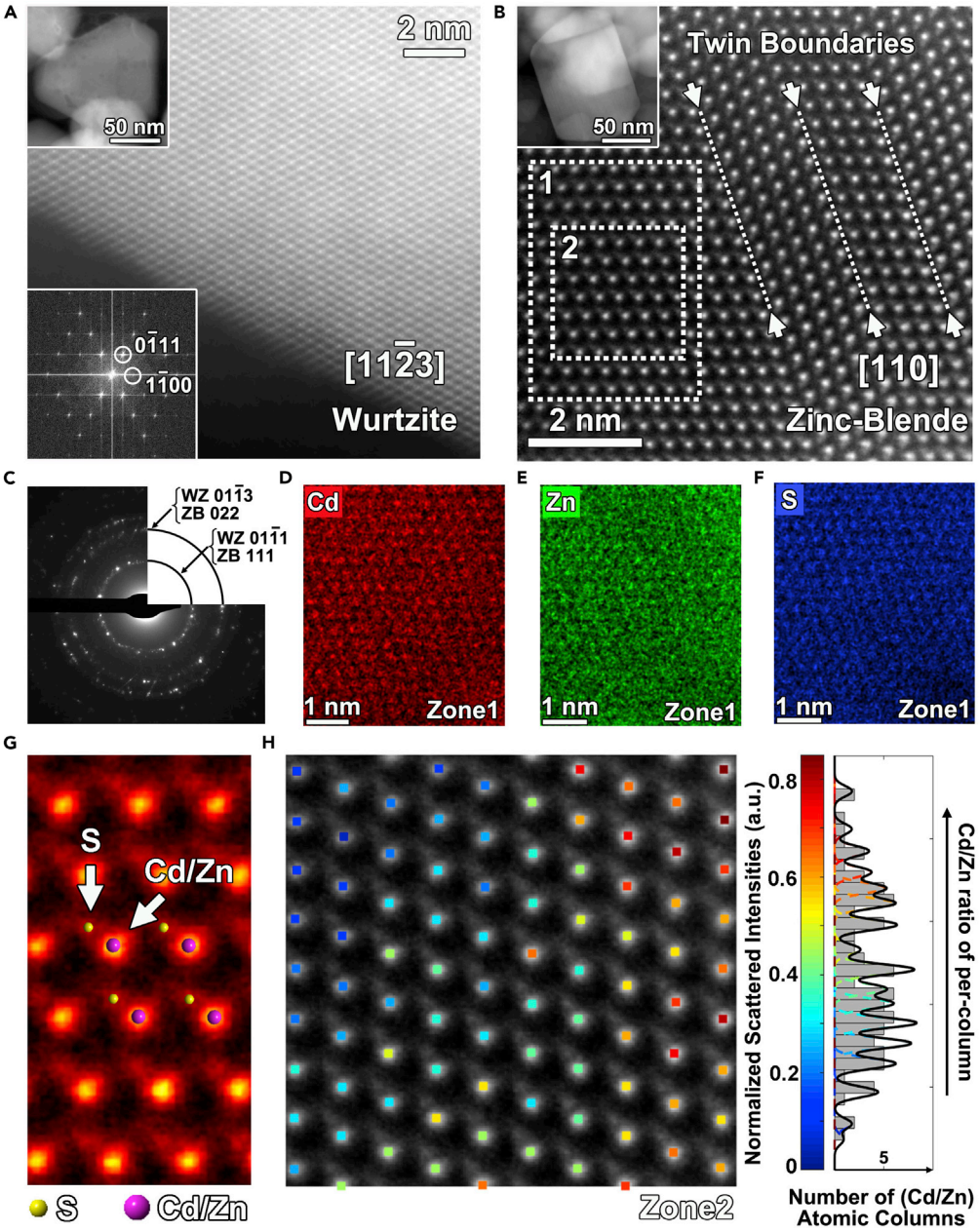

Figure 2. Structure characterization of $Zn_{0.6}Cd_{0.4}S$

(A) HR-HAADF-STEM image of the WZ phase, corresponding FFT (lower inset), and a low magnification STEM image (upper inset).

(B) HR-HAADF-STEM image of the ZB phase and corresponding low magnification STEM image (inset).

(C) SAED pattern over a large area for $Zn_{0.6}Cd_{0.4}S$.

(D–F) corresponding EDS elemental maps of zone 1 in (B) indicated by the white dashed box: Cd (red), Zn (green), and S (blue).

(G) Enlarged HR-HAADF-STEM image in (B) together with the ZB crystal model.

(H) Atomic resolution HAADF-STEM image of zone 2 in (B) with quantitative scattered intensities per Cd/Zn column and corresponding histogram of the normalized scattered intensities of the Cd/Zn atomic columns.

$Zn_{1-x}Cd_xS$ solid solution gradually changes from WZ to ZB structure. The average crystallite size of $Zn_{1-x}Cd_xS$ samples was estimated by using the Scherrer equation, and the calculated values are listed in Table 1. The surface/subsurface (~10 nm) chemical composition and electronic states such as binding

Table 1. Structural characteristics of $Zn_{1-x}Cd_xS$ and photocatalytic performance for glucose conversion

X value	Bandgap (eV)	Zeta potential (mV)	Crystallite size (nm)	S_{BET} ($m^2 \cdot g^{-1}$)	H_2 evolution rate ($\mu mol \cdot h^{-1} \cdot g^{-1}$)	Glucose conversion (%)	Lactic acid selectivity (%)	Carbon balance (%)
0	3.55	−4.0 ± 0.1	35.1	14.2	24.6 ± 1.23	64.6 ± 1.53	58.8 ± 1.44	70.5 ± 2.92
0.2	2.91	−5.9 ± 0.6	25.5	11.7	378 ± 15.1	81.4 ± 0.51	76.4 ± 2.84	74.5 ± 3.47
0.4	2.55	−8.7 ± 0.2	12.7	13.7	690 ± 27.6	87.8 ± 0.95	75.9 ± 0.91	51.4 ± 4.66
0.6	2.45	−14.4 ± 0.5	15.3	14.0	404 ± 16.2	78.0 ± 1.08	58.1 ± 0.92	54.1 ± 3.40
0.8	2.35	−15.8 ± 0.7	29.9	16.0	391 ± 15.7	78.2 ± 0.80	68.8 ± 1.20	62.0 ± 2.42
1.0	2.25	−16.9 ± 0.6	35.9	12.1	113 ± 5.67	83.2 ± 0.68	85.8 ± 0.68	91.3 ± 3.54

energy and oxidation state of the as-fabricated samples were investigated by X-ray photoelectron spectroscopy (XPS) (Figure S8). A peak separation of 23.0 eV due to spin-orbit splitting confirm that the Zn element existed as Zn^{2+}(Al-Gaashani, et al., 2013). Interestingly, $Zn_{1-x}Cd_xS$ samples with Cd^{2+} exhibit a slight increase in the binding energy of the Zn^{2+} that might be due to redistribution of charge on Zn atom in variable crystalline phase (Figure S9B). The deconvoluted XPS signal at 405.0 and 411.8 eV is raised due to the $Cd3d_{5/2}$ and $Cd3d_{3/2}$ peak components of Cd^{2+} in the well-crystallized CdS nanostructure. Other shoulder peaks at higher binding energy (BE) around 406.1 and 412.9 eV can be ascribed to the surface Cd atoms with an unsaturated coordination as surface atoms are known to have a slight blue shift in binding energy with respect to the bulk value (Figure S8C).(Wei, et al., 2012; Winkler, et al., 1999) As expected, after the formation of the homojunctions, the BE of the Cd3d peak components slightly shifts toward lower binding energy due to the storage of some charge in the homojunctions (Figure S9C).

Hydrogen production from glucose photocatalysis

To this end, the photocatalytic hydrogen production from $Zn_{1-x}Cd_xS$ in the presence of glucose has been assessed. The time course of the H_2 production during a 5 hr irradiation under visible light (300 W Xenon lamp) in a 1 M NaOH solution shows an almost linear relation for all the samples (Figure S10). Pure CdS or ZnS shows a much lower H_2 production rate while samples with both Zn and Cd exhibit a higher performance reaching a maximum for $Zn_{0.6}Cd_{0.4}S$ (690 ± 27.6 $\mu mol \cdot h^{-1} \cdot g_{catalyst}^{-1}$) in a 20 g/L glucose solution (Figure 3A). The H_2 production rates are consistent with the photocurrent density as measured by a standard three-electrode system, indicating the presence of ZB-WZ TSL with a homojunction structure indeed enhances the separation efficiency of photogenerated electrons and holes (Figure 3B). Additionally, $Zn_{0.6}Cd_{0.4}S$ exhibits a high stability for H_2 production without any significant performance loss even after 20 hr irradiation (Figures 3C and S11A). The high photostability could come from the formation of corresponding metal oxides on the photocatalyst surface, which suppress the photo-corrosion from the breakage of chemical bonds between sulfur and metals by photogenerated holes (Wakerley, et al., 2017). The glucose concentration was further optimized based on the H_2 production activity and a 20 g/L glucose solution was found to be the ideal concentration (Figure S11B). The presence of alkali could suppress the photo-corrosion of $Zn_{1-x}Cd_xS$ by forming oxides on the surface and facilitate glucose conversion by deprotonation effect (Wakerley, et al., 2017; Jin, et al., 2017). Therefore, we investigated the effects of alkalinity on H_2 generation with optimized glucose concentration (Figure S11C). The suspension in KP_i (pH 7) shows a negligible H_2 generation, and the color turns to black after 5 hr irradiation, indicating a severe photo-corrosion of $Zn_{1-x}Cd_xS$ without the addition of NaOH (Figure S12).

To probe the performance of the catalyst in the longer wavelength region, the solar-to-hydrogen conversion rate was evaluated by measuring the photocatalytic H_2 production under different monochromatic lights, and the apparent quantum yields (AQYs) were then calculated over the photocatalyst $Zn_{0.6}Cd_{0.4}S$ (Figure 3D). The AQYs of $Zn_{0.6}Cd_{0.4}S$ follow the UV-Vis absorption profile consistent with the light absorbance in the visible light region. To understand the photocatalytic H_2 production mechanism, the electronic properties of $Zn_{1-x}Cd_xS$ were then studied by density functional theory (DFT). The DFT results indicate that the valence bands below the Fermi level are mainly constituted of S orbitals while the conduction bands above the Fermi level are contributed by S, Cd, or Zn and vary with the doping level (Figure S13). Even though, ZnS has the largest reduction ability (Figure 1C), a large ΔG indicates that it is not an active hydrogen evolution reaction (HER) catalyst. These results agree with the experimental measurements (Figure S14). Protons tend to bind on Cd in pure CdS with a ΔG of around −2.48 eV while in the $Zn_{1-x}Cd_xS$ solid solutions, the H tends to bind on S

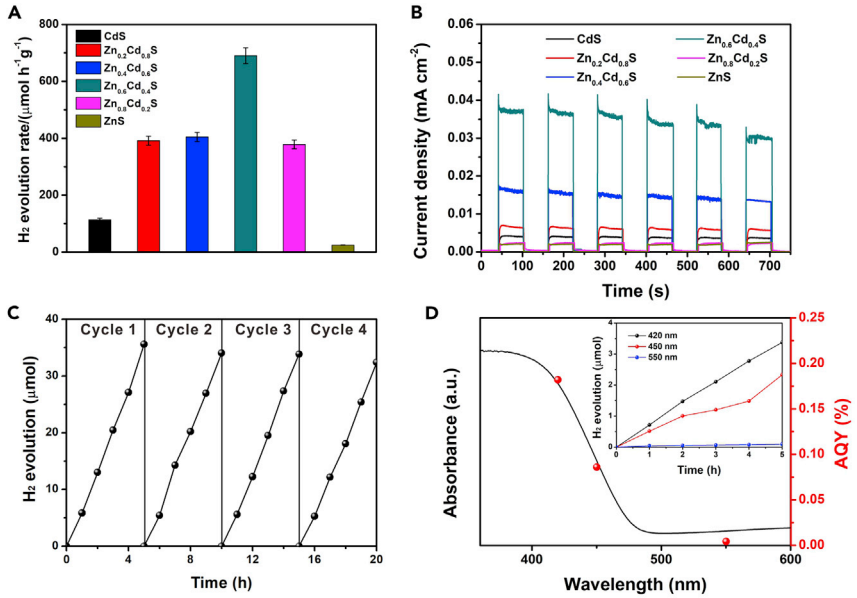

Figure 3. Hydrogen production from glucose photoreforming

(A) Photocatalytic hydrogen evolution rates of $Zn_{1-x}Cd_xS$ solid solutions in 20 g/L glucose solution.

(B) Photocurrent densities of $Zn_{1-x}Cd_xS$ solid solutions.

(C) Photocatalytic stability of $Zn_{0.6}Cd_{0.4}S$.

(D) UV-vis absorbance spectrum and corresponding AQY values of Zn0.6Cd0.4S calculated from the hydrogen generation performance (inset). Data are represented as mean ± standard error of the mean, and error bars in (A) are representative of three independent experiments.

atoms with a little smaller ΔG and favors better performance. Therefore, $Zn_{1-x}Cd_xS$ solid solutions with bandgap engineering provide an enhancement in HER performance.

Glucose conversion and products analysis

Besides of the hydrogen generation, the beauty of biomass/glucose photoreforming is the co-generation of value-added bioproducts instead of CO_2 in the liquid phase. It is widely acknowledged that glucose will be quickly isomerized into fructose in alkaline solution (Montejo-Valencia and Curet-Arana, 2019). We observed that approximately 50% of initial glucose was isomerized immediately in 1.0 M NaOH solution before irradiation, and this isomerization equilibrium was kept stable without catalysts (Figure S15). Taking the glucose consumption by alkali into account, different $Zn_{1-x}Cd_xS$ photocatalysts showed variable glucose conversion rate that indicated that the bandgap engineering indeed affects the glucose oxidation (Figure 4A). Lactic acid and formic acid were the major liquid products obtained from photocatalytic glucose conversion where the concentration of lactic acid gradually increased along with the consumption of glucose (Figures 4B and S16). The lactic acid selectivity and yield were separately calculated and presented in Table 1 and Figure S17. Further oxidation of generated lactic acid and formic acid is protected and can be explained based on their existence as negatively charged lactate and formate ion under alkaline condition preventing adsorption on negatively charge surface catalyst as verified by negative zeta potential (Table 1). This was further evidenced by directly adding lactic acid and formic acid in the photocatalytic reaction system, which have remained stable during course of the reaction (Figure S18). Noticeably, CO_2 or carbonate was not detected in gas-phase and liquid-phase products, indicating that the designed $Zn_{1-x}Cd_xS$ photocatalysts inhibited the over-oxidation of glucose. Besides, it could also be noticed that $Zn_{0.6}Cd_{0.4}S$ maximized the hydrogen production and glucose conversion which is due to the synergistic effect of light absorbance, charge separation, and redox ability. However, CdS (x = 1 for $Zn_{1-x}Cd_xS$) exhibited highest lactic acid selectivity, and the irregularity of lactic acid selectivity along with x value may also originate from multiple effects of the photocatalysts.

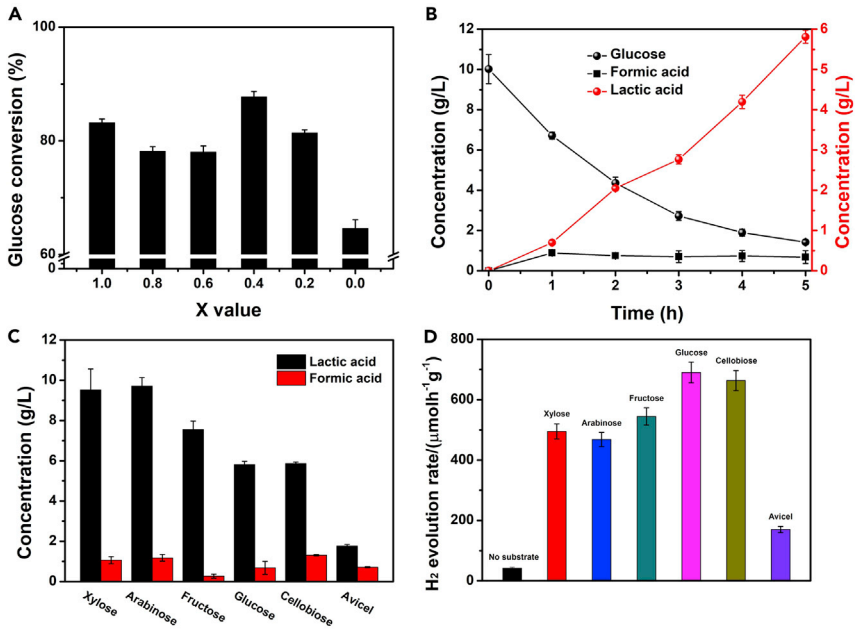

Figure 4. Glucose conversion and product analysis

(A) Glucose conversion over $Zn_{1-x}Cd_xS$ solid solutions.

(B) Concentration of glucose, formic acid, and lactic acid during the photocatalytic reaction over $Zn_{0.6}Cd_{0.4}S$.

(C and D) (C) Lactic acid and formic acid production and (D) hydrogen production from different substrates over $Zn_{0.6}Cd_{0.4}S$. Data are represented as mean ± standard error of the mean, and error bars are representative of three independent experiments.

To further explore the potential of the catalyst toward biomass photoreforming, we further tested the photocatalytic performance of band-engineered $Zn_{0.6}Cd_{0.4}S$ catalyst with homojunction structure for other monosaccharides (xylose, arabinose, and fructose), disaccharides (cellobiose), and polysaccharides (Avicel: cellulose microcrystalline). Similar as glucose, all these saccharides produced lactic acid and formic acid after the photocatalytic reaction (Figure 4C). The higher lactic acid yield for pentoses (xylose and arabinose) than hexoses (fructose and glucose) indicates pentoses are easier to be converted into lactic acid than hexoses. Considering steric hindrance, cellobiose, a D-glucose dimer linked by β-O-4 glycosidic bond, was expected to show much reduced activity than glucose. Surprisingly, cellobiose displayed almost identical lactic acid production efficiency as glucose (Figure 4C). This was likely due to the fact that cellobiose could be quickly converted into glucose and fructose under the alkaline condition and the actual substrates during the photocatalysis of cellobiose in our system were glucose and fructose (Bonn, et al., 1985). As expected, the glucose polysaccharide (Avicel) with even more complex intramolecular and stronger inter/intra molecular hydrogen bonding showed much lower lactic acid production. On the other hand, H_2 productions from these saccharides were also simultaneously investigated (Figure 4D). Negligible H_2 production (41.8 ± 3.34 $\mu mol \cdot h^{-1} \cdot g_{cat.}^{-1}$) was observed over $Zn_{0.6}Cd_{0.4}S$ homojunction in the absence of any substrate. While the H_2 production activities were significantly enhanced when saccharides were added into the system, they could consume the photogenerated holes on $Zn_{0.6}Cd_{0.4}S$ homojunction photocatalysts. Again, Avicel exhibited much lower hydrogen production than that of other monosaccharides and disaccharide due to the more complex structure.

Active species and proposed mechanism

To trace the active species for glucose photocatalytic conversion, different scavengers ethylenediaminetetraacetic acid (EDTA), *p*-benzoquinone (BQ), and isopropyl alcohol (IPA) were added into the reaction system to elucidate the roles of photogenerated holes (h^+), superoxide radical anion ($\cdot O_2^-$), and hydroxyl radical (·OH), respectively. IPA strongly inhibited glucose conversion which indicated that ·OH is the main active species dominating the glucose conversion (Figure 5A). The O_2^- also contributed to a less extent as the addition of BQ slightly suppressed glucose conversion. According to previous studies, ·OH in the reaction system can be produced by (i) oxidation of absorbed H_2O molecule or hydroxide

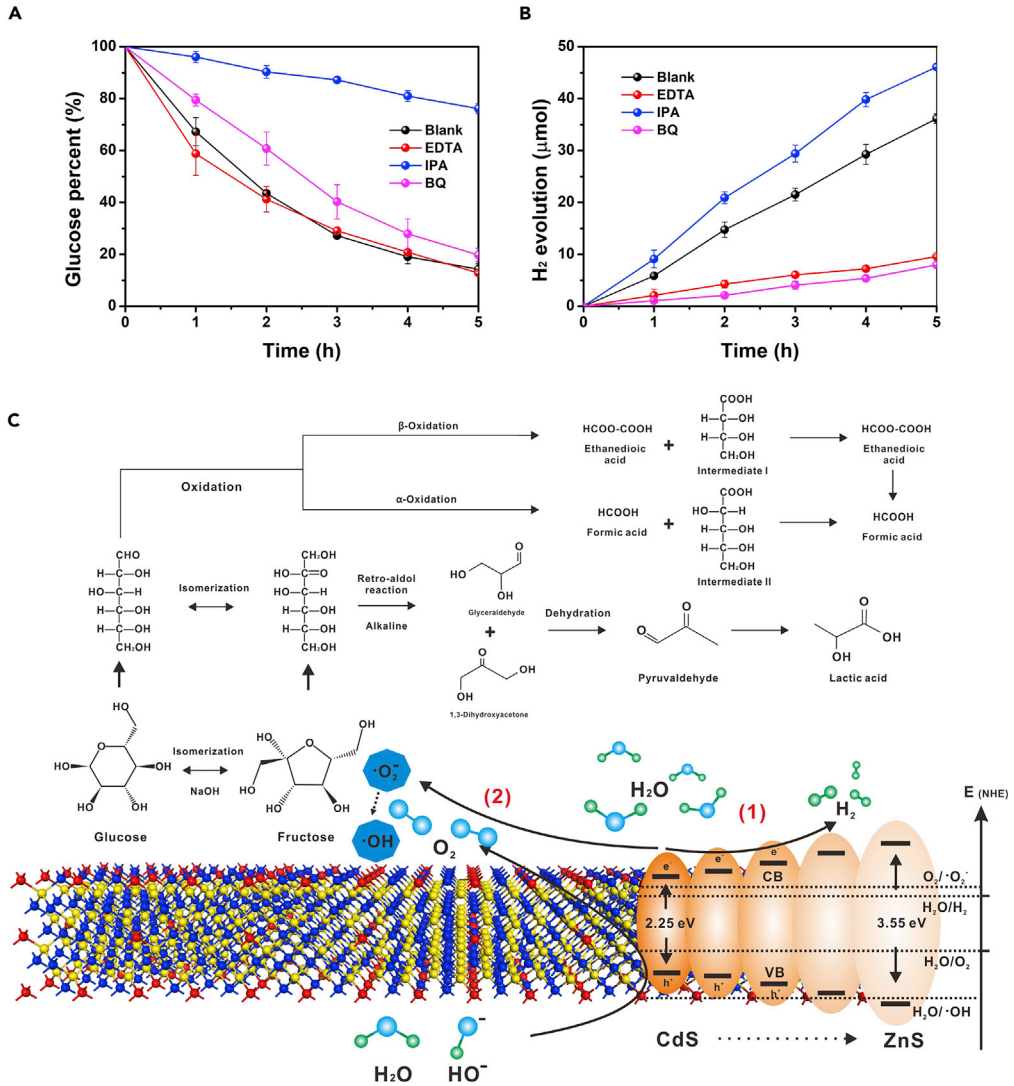

Figure 5. Investigation of active species and proposed mechanism

(A) The effect of different scavengers (EDTA, IPA, and BQ) on solar-light-driven glucose conversion.

(B and C) (B) Hydrogen production activity. The concentrations of EDTA and BQ were 1.0 mmol·L-1, and 3.2 mmol·L-1 for IPA and (C) proposed reaction pathway for glucose photocatalysis. Data are represented as mean ± standard error of the mean, and error bars in (A) and (B) are representative of three independent experiments.

ions on the photocatalyst surface by photo-generated holes or (ii) derivation from $\cdot O_2^-$ via hydroperoxide radical and hydrogen peroxide intermediate or (iii) atomic oxygen species (Mailloux, 2015; Herrmann, 2001). Since the addition of EDTA to consume the h^+ showed no effect on glucose conversion and a similar result was observed when triethanolamine was used as another hole scavenger (Figure S19), the presence of ·OH in the reaction system should be derived from $\cdot O_2^-$. Herein, the rate-determining step of glucose photocatalysis is the derivation of $\cdot O_2^-$ to ·OH, followed by the oxidation reaction triggered from ·OH. The $\cdot O_2^-$ species is produced by the reduction of catalyst surface absorbed O_2 by photogenerated electrons. The required O_2 could come from the dissolved air in the water and/or oxidation of absorbed H_2O molecules or hydroxide ions by photogenerated holes. The hydrogen production activity further revealed that the consumption of ·OH enhanced the proton reduction reaction (Figure 5B). To further prove the presence of $\cdot O_2^-$ to ·OH during the photocatalytic reaction, electron spin resonance (ESR) was performed by using 5,5-dimethyl-1-pyrroline N-oxide as the ESR spin label for the detection of $\cdot O_2^-$ and ·OH while 2,2,6,6-tetramethyl-4-piperidone-1-oxyl for singlet excited state oxygen ($^1O_2$) (Figure S20). The results

demonstrate that the photocatalyst of $Zn_{0.6}Cd_{0.4}S$ indeed produces $\cdot O_2^-$ and ·OH during the photocatalytic reaction, and these active oxygen species correspond to the glucose conversion.

Combining our results and previous studies, we proposed a possible mechanism for glucose photocatalysis with band-engineered $Zn_{0.6}Cd_{0.4}S$ homojunction (Figure 5C).(Holm, et al., 2010; Wang, et al., 2013; Liu et al., 2020a, 2020b) Under visible light irradiation, $Zn_{1-x}Cd_xS$ homojunction possessing a favorable bandgap is activated, and the photogenerated electrons on the conduction band reduce the absorbed oxygen to form superoxide radicals. The generated superoxide radical undergoes the further derivatization process via hydroperoxide radical to produce other reactive oxygen species such as ·OH. These active ·OH species initiate the conversion of glucose to final lactic acid. The process of glucose to lactic acid under alkali condition during the photocatalytic reaction firstly involves the isomerization of glucose to fructose along with ring-opening reactions of glucose and fructose. Then, the hydrolysis (retro-aldol) reaction of fructose produces glyceraldehyde and 1, 3-dihydroxyacetone under the effect of active oxygen species. Pyruvaldehyde is then obtained after the dehydration process, and lactic acid is finally produced after a series of steps. Besides, the detected formic acid is probably from the α- and/or β-oxidation reaction of glucose. As lactic acid and formic acid exist in the form of anions-lactate and formate and the photocatalysts possess negative charge surface properties, lactate and formate cannot be adsorbed on the photocatalyst surface. Thus, lactic acid and formic acid are the final products from glucose photocatalysis over a $Zn_{1-x}Cd_xS$ solid solution under alkaline conditions.

CONCLUSION

In summary, a bandgap engineering strategy of a $Zn_{1-x}Cd_xS$ solid solution with ZB-WZ homojunctions has been investigated to convert glucose to lactic acid and H_2 by photocatalysis. The twinning superlattice in the as-fabricated photocatalyst improves the separation efficiency of the photogenerated electrons and holes while bandgap engineering is important to enhance the hydrogen production. The photocatalysts demonstrated a high glucose conversion (~90%) and lactic acid selectivity (~87%), as well as an excellent H_2 generation (690 $\pm$ 27.6 $\mu mol \cdot h^{-1} \cdot g_{cat.}^{-1}$), without any co-catalyst under visible-light irradiation. The reaction pathway was proposed based on the results, and the $\cdot O_2^-$ was found to be the key species for lactic acid production from glucose photoreforming. This work is shining new light on efficiently converting saccharides or even biomass to produce sustainable hydrogen fuel and high value-added products by designing novel photocatalysts.

Limitations of the study

This study has demonstrated the bandgap engineering of $Zn_{1-x}Cd_xS$ solid solution photocatalysts with homojunctions for efficient glucose conversion. Experimental results suggested that the photocatalysts had good glucose conversion and excellent lactic acid selectivity as well as considerable H_2 generation. However, the in-depth understanding of photocatalytic mechanism is still needed by further in-situ characterization and DFT calculations, especially for the exact roles of photogenerated electrons and holes during the multiple reaction pathways of glucose and intermediates. We will keep working on related projects by using more advanced technologies to better understand the in-depth mechanism.

Resource availability

Lead contact

Further information and requests for resources should be directed to and will be fulfilled by the lead contact, Jinguang Hu (jinguang.hu@ucalgary.ca).

Material availability

Full experimental and spectroscopy measurement details can be found in the Supplemental Information.

Data and code availability

All data supporting this study are available in the Manuscript and Supplemental Information.

METHODS

All methods can be found in the accompanying Transparent Methods supplemental file.

SUPPLEMENTAL INFORMATION

Supplemental information can be found online at https://doi.org/10.1016/j.isci.2021.102109.

ACKNOWLEDGMENTS

This work is financially supported by the Canada First Research Excellence Fund (CFREF), Natural Science Foundation of Hubei Province (2020CFB416), and the Fundamental Research Funds for the Central Universities (WUT: 2020III002GX).

AUTHOR CONTRIBUTIONS

Heng Zhao: Methodology, Investigation, Writing-original draft, Writing-review & editing. **Chao-Fan Li:** Investigation-TEM characterization. **Xue Yong:** Investigation-DFT calculation. **Pawan Kumar:** Writing-review & editing. **Bruna Palma:** Investigation-GC-MS analysis. **Zhi-Yi Hu:** Resources, Investigation-TEM characterization, Writing-review & editing. **Gustaaf Van Tendeloo:** Resources-TEM, Writing-review & editing. **Samira Siahrostami:** Investigation-DFT calculation and Writing-review & editing. **Stephen Larter:** Resources-GC-MS, Writing-review & editing. **Dewen Zheng:** Writing-review & editing. **Shanyu Wang:** Writing-review & editing. **Zhangxin Chen:** Funding acquisition. **Md Golam Kibria:** Supervision, Validation, Writing-review & editing. **Jinguang Hu:** Supervision, Validation, Writing-review & editing, Funding acquisition.

DECLARATION OF INTERESTS

The authors declare no competing interests.

Received: December 9, 2020
Revised: January 5, 2021
Accepted: January 20, 2021
Published: February 19, 2021

REFERENCES

Van Aert, S., Verbeeck, J., Erni, R., Bals, S., Luysberg, M., Van Dyck, D., and Van Tendeloo, G. (2009). Quantitative atomic resolution mapping using high-angle annular dark field scanning transmission electron microscopy. Ultramicroscopy *109*, 1236–1244.

Al-Gaashani, R., Radiman, S., Daud, A.R., Tabet, N., and Al-Douri, Y. (2013). XPS and optical studies of different morphologies of ZnO nanostructures prepared by microwave methods. Ceram. Int. *39*, 2283–2292.

Algra, R.E., Verheijen, M.A., Borgstrom, M.T., Feiner, L.F., Immink, G., van Enckevort, W.J.P., Vlieg, E., and Bakkers, E.P.A.M. (2008). Twinning superlattices in indium phosphide nanowires. Nature *456*, 369–372.

Asahi, R., Morikawa, T., Irie, H., and Ohwaki, T. (2014). Nitrogen-doped titanium dioxide as visible-light-sensitive photocatalyst: designs, developments, and prospects. Chem. Rev. *114*, 9824–9852.

Backer, De, van den Bos, K.H.W., Van den Broek, W., Sijbers, J., and Van Aert, S. (2016). StatSTEM: an efficient approach for accurate and precise model-based quantification of atomic resolution electron microscopy images. Ultramicroscopy *171*, 104–116.

Bonn, G., Binder, H., Leonhard, H., and Bobleter, O. (1985). The alkaline-degradation of cellobiose to glucose and fructose. Monatsh Chem. *116*, 961–971.

Butburee, T., Chakthranont, P., Phawa, C., and Faungnawakij, K. (2020). Beyond artificial photosynthesis: prospects on photobiorefinery. ChemCatChem *12*, 1873–1890.

Chaves, Azadani, J.G., Alsalman, H., da Costa, D.R., Frisenda, R., Chaves, A.J., Song, S.H., Kim, Y.D., He, D.W., Zhou, J.D., et al. (2020). Bandgap engineering of two-dimensional semiconductor materials. Npj 2d Mater. Appl. *4*, 1–21.

Choi, W.Y., Termin, A., and Hoffmann, M.R. (1994). The role of metal-ion dopants in quantum-sized TiO_2 - correlation between photoreactivity and charge-carrier recombination dynamics. J. Phys. Chem. *98*, 13669–13679.

Ding, Q.Q., Zhang, Y., Chen, X., Fu, X.Q., Chen, D.K., Chen, S.J., Gu, L., Wei, F., Bei, H.B., Gao, Y.F., et al. (2019). Tuning element distribution, structure and properties by composition in high-entropy alloys. Nature *574*, 223–227.

Duan, Q.Q., Ji, J.Y., Hong, X., Fu, Y.C., Wang, C.Y., Zhou, K., Liu, X.Q., Yang, H., and Wang, Z.Y. (2020). Design of hole-transport-material free $CH_3NH_3PbI_3$/$CsSnI_3$ all-perovskite heterojunction efficient solar cells by device simulation. Sol. Energy *201*, 555–560.

Herrmann, J.M. (2001). Active agents in heterogeneous photocatalysis: atomic oxygen species vs. OH(.) radicals: related quantum yields. Helv. Chim. Acta *84*, 2731–2750.

Holm, M.S., Saravanamurugan, S., and Taarning, E. (2010). Conversion of sugars to lactic acid derivatives using heterogeneous zeotype catalysts. Science *328*, 602–605.

Holmes, M.A., Townsend, T.K., and Osterloh, F.E. (2012). Quantum confinement controlled photocatalytic water splitting by suspended CdSe nanocrystals. Chem. Commun. *48*, 371–373.

Huber, G.W., Iborra, S., and Corma, A. (2006). Synthesis of transportation fuels from biomass: chemistry, catalysts, and engineering. Chem. Rev. *106*, 4044–4098.

Iervolino, G., Vaiano, V., Sannino, D., Rizzo, L., and Palma, V. (2017). Enhanced photocatalytic hydrogen production from glucose aqueous matrices on Ru-doped $LaFeO_3$. Appl. Catal. B Environ. *207*, 182–194.

Jacopin, G., Rigutti, L., Largeau, L., Fortuna, F., Furtmayr, F., Julien, F.H., Eickhoff, M., and Tchernycheva, M. (2011). Optical properties of wurtzite/zinc-blende heterostructures in GaN nanowires. J. Appl. Phys. *110*, 064313.

Jin, B.B., Yao, G.D., Wang, X.G., Ding, K.F., and Jin, F.M. (2017). Photocatalytic oxidation of glucose into formate on nano TiO_2 catalyst. ACS Sustain. Chem. Eng. *5*, 6377–6381.

Jin, B., Liang, F., Hu, Z.Y., Wei, P., Liu, K.L., Hu, X.Z., Van Tendeloo, G., Lin, Z.S., Li, H.Q., Zhou, X., et al. (2020). Nonlayered CdSe flakes homojunctions. Adv. Funct. Mater. *30*, 1908902.

Klenov, D.O., and Stemmer, S. (2006). Contributions to the contrast in experimental

high-angle annular dark-field images. Ultramicroscopy *106*, 889–901.

Komesu, J.A.R.de Oliveira, Martins, L.H.D., Maciel, M.R.W., and Maciel, R. (2017). Lactic acid production to purification: a review. Bioresources *12*, 4364–4383, Komesu.

Liu, M.C., Jing, D.W., Zhou, Z.H., and Guo, L.J. (2013). Twin-induced one-dimensional homojunctions yield high quantum efficiency for solar hydrogen generation. Nat. Commun. *4*, 1–8.

Liu, W.J., Xu, Z., Zhao, D., Pan, X.Q., Li, H.C., Hu, X., Fan, Z.Y., Wang, W.K., Zhao, G.H., Jin, S., et al. (2020a). Efficient electrochemical production of glucaric acid and H_2 via glucose electrolysis. Nat. Commun. *11*, 265.

Liu, M., Qiao, L.Z., Dong, B.B., Guo, S., Yao, S., Li, C., Zhang, Z.M., and Lu, T.B. (2020b). Photocatalytic coproduction of H_2 and industrial chemical over MOF-derived direct Z-scheme heterostructure. Appl. Catal. B Environ. *273*, 119066.

Mailloux, R.J. (2015). Teaching the fundamentals of electron transfer reactions in mitochondria and the production and detection of reactive oxygen species. Redox Biol. *4*, 381–398.

Maki-Arvela, P., Simakova, I.L., Salmi, T., and Murzin, D.Y. (2014). Production of lactic acid/lactates from biomass and their catalytic transformations to commodities. Chem. Rev. *114*, 1909–1971.

Mayer, M.T., Lin, Y.J., Yuan, G.B., and Wang, D.W. (2013). Forming heterojunctions at the nanoscale for improved photoelectrochemical water splitting by semiconductor materials: case studies on hematite. Acc. Chem. Res. *46*, 1558–1566.

Montejo-Valencia, B.D., and Curet-Arana, M.C. (2019). Periodic DFT study of the opening of fructose and glucose rings and the further conversion of fructose to trioses catalyzed by M-BEA (M = Sn, Ti, Zr, or Hf). J. Phys. Chem. C *123*, 3532–3540.

Nguyen, V.C., Ke, N.J., Nam, L.D., Nguyen, B.S., Xiao, Y.K., Lee, Y.L., and Teng, H.S. (2019). Photocatalytic reforming of sugar and glucose into H_2 over functionalized graphene dots. J. Mater. Chem. A *7*, 8384–8393.

Ning, C.Z., Dou, L.T., and Yang, P.D. (2017). Bandgap engineering in semiconductor alloy nanomaterials with widely tunable compositions. Nat. Rev. Mater. *2*, 17070.

Pemasiri, K., Montazeri, M., Gass, R., Smith, L.M., Jackson, H.E., Yarrison-Rice, J., Paiman, S., Gao, Q., Tan, H.H., Jagadish, C., et al. (2009). Carrier dynamics and quantum confinement in type II ZB-WZ InP nanowire homostructures. Nano Lett. *9*, 648–654.

Pennycook, S.J., and Jesson, D.E. (1991). High-resolution Z-contrast imaging of crystals. Ultramicroscopy *37*, 14–38.

Ragauskas, A.J., Williams, C.K., Davison, B.H., Britovsek, G., Cairney, J., Eckert, C.A., Frederick, W.J., Hallett, J.P., Leak, D.J., Liotta, C.L., et al. (2006). The path forward for biofuels and biomaterials. Science *311*, 484–489.

Ricolleau, C., Audinet, L., Gandais, M., and Gacoin, T. (1999). Structural transformations in II-VI semiconductor nanocrystals. Eur. Phys. J. D *9*, 565–570.

Rubin, E.M. (2008). Genomics of cellulosic biofuels. Nature *454*, 841–845.

Sang, X.H., and LeBeau, J.M. (2014). Revolving scanning transmission electron microscopy: correcting sample drift distortion without prior knowledge. Ultramicroscopy *138*, 28–35.

Schneider, J., and Bahnemann, D.W. (2013). Undesired role of sacrificial reagents in photocatalysis. J. Phys. Chem. Lett. *4*, 3479–3483.

Wakerley, D.W., Kuehnel, M.F., Orchard, K.L., Ly, K.H., Rosser, T.E., and Reisner, E. (2017). Solar-driven reforming of lignocellulose to H_2 with a CdS/CdO_x photocatalyst. Nat. Energy *2*, 17021.

Wang, Y.L., Deng, W.P., Wang, B.J., Zhang, Q.H., Wan, X.Y., Tang, Z.C., Wang, Y., Zhu, C., Cao, Z.X., Wang, G.C., and Wan, H.L. (2013). Chemical synthesis of lactic acid from cellulose catalysed by lead(II) ions in water. Nat. Commun. *4*, 1–7.

Wei, H.H.Y., Evans, C.M., Swartz, B.D., Neukirch, A.J., Young, J., Prezhdo, O.V., and Krauss, T.D. (2012). Colloidal semiconductor quantum dots with tunable surface composition. Nano Lett. *12*, 4465–4471.

Winkler, U., Eich, D., Chen, Z.H., Fink, R., Kulkarni, S.K., and Umbach, E. (1999). Thermal behaviour of CdS nanoparticles investigated by high resolution photoelectron spectroscopy. Physica Status Solidi *173*, 253–259.

Wu, Q., He, Y.M., Zhang, H.L., Feng, Z.Y., Wu, Y., and Wu, T.H. (2017). Photocatalytic selective oxidation of biomass-derived 5-hydroxymethylfurfural to 2,5-diformylfuran on metal-free g-C_3N_4 under visible light irradiation. Mol. Catal. *436*, 10–18.

Wu, X.X., Zhao, H., Khan, M.A., Maity, P., Al-Attas, T., Larter, S., Yong, Q., Mohammed, O.F., Kibria, M.G., and Hu, J.G. (2020a). Sunlight-driven biomass photorefinery for coproduction of sustainable hydrogen and value-added biochemicals. ACS Sustain. Chem. Eng. *8*, 15772–15781.

Wu, J.J., Shen, L.Y., Duan, S., Chen, Z.N., Zheng, Q.S., Liu, Y.Q., Sun, Z.M., Clark, J.H., Xu, X., and Tu, T. (2020b). Selective catalytic dehydrogenative oxidation of bio-polyols to lactic acid. Angew. Chem. Int. Edit. *59*, 13871–13878.

Zhang, Z.H., and Huber, G.W. (2018). Catalytic oxidation of carbohydrates into organic acids and furan chemicals. Chem. Soc. Rev. *47*, 1351–1390.

Zhang, H.L., Wu, Q., Guo, C., Wu, Y., and Wu, T.H. (2017a). Photocatalytic selective oxidation of 5-hydroxymethylfurfural to 2,5-diformylfuran over Nb_2O_5 under visible light. ACS Sustain. Chem. Eng. *5*, 3517–3523.

Zhang, K., Dai, Y.W., Zhou, Z.H., Jan, S.U., Guo, L.J., and Gong, J.R. (2017b). Polarization-induced saw-tooth-like potential distribution in zincblende-wurtzite superlattice for efficient charge separation. Nano Energy *41*, 101–108.

Zhao, H., Li, C.F., Liu, L.Y., Palma, B., Hu, Z.Y., Renneckar, S., Larter, S., Li, Y., Kibria, M.G., Hu, J., and Su, B.L. (2021). n-p Heterojunction of TiO_2-NiO core-shell structure for efficient hydrogen generation and lignin photoreforming. J. Colloid Interf. Sci. *585*, 694–704.

iScience, Volume *24*

Supplemental Information

Coproduction of hydrogen and lactic acid from glucose photocatalysis on band-engineered $Zn_{1-x}Cd_xS$ homojunction

Heng Zhao, Chao-Fan Li, Xue Yong, Pawan Kumar, Bruna Palma, Zhi-Yi Hu, Gustaaf Van Tendeloo, Samira Siahrostami, Stephen Larter, Dewen Zheng, Shanyu Wang, Zhangxin Chen, Md Golam Kibria, and Jinguang Hu

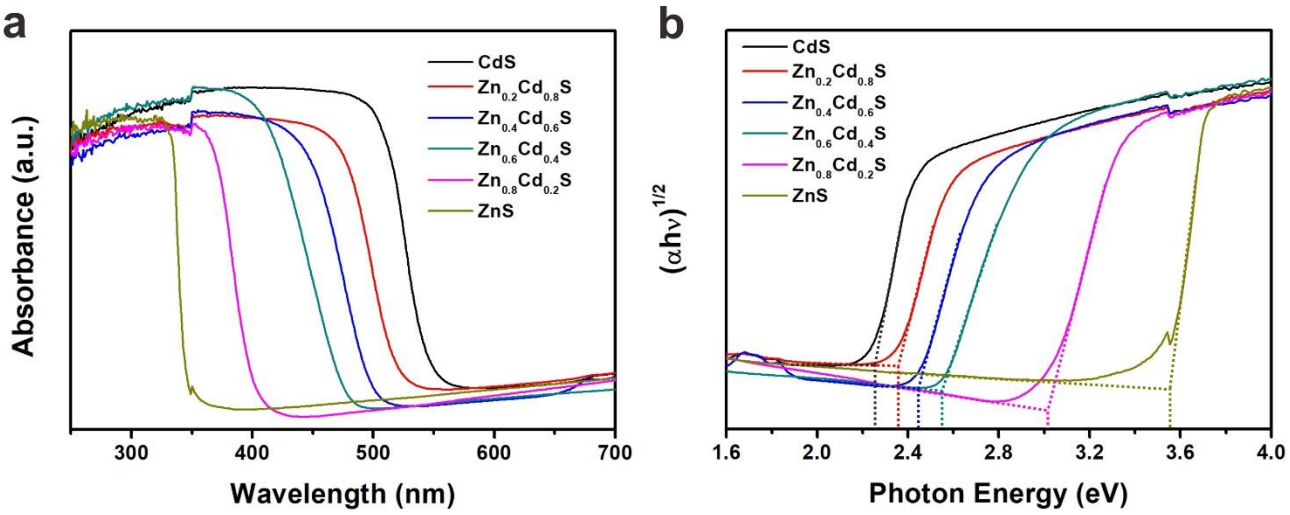

Figure S1 Optical properties (Related to Figure 1). (a) UV-vis diffuse reflectance spectra and (b) corresponding Tauc plot of $Zn_{1-x}Cd_xS$ solid solutions with different x values.

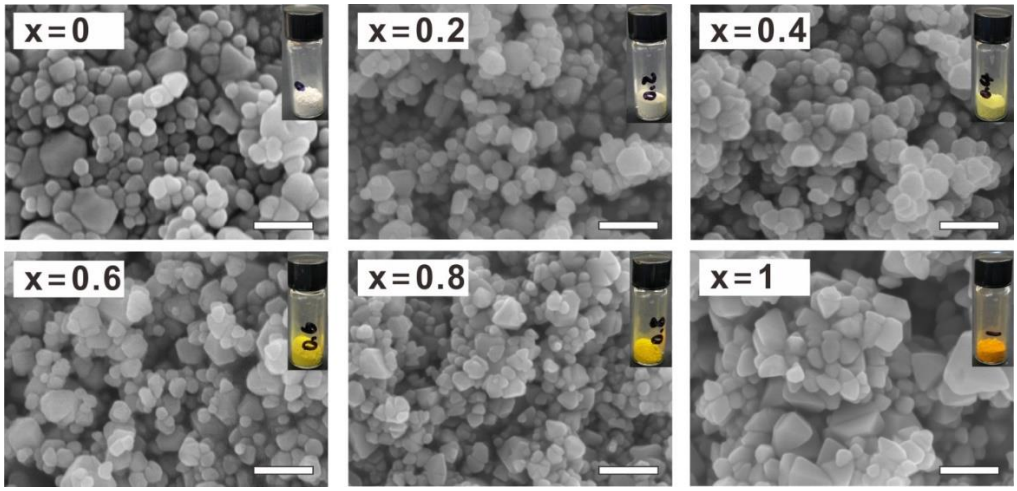

Figure S2 Mophology characterization (Related to Figure 2). SEM images and photographs of $Zn_{1-x}Cd_xS$ solid solutions with different x values (scale bar: 200 nm).

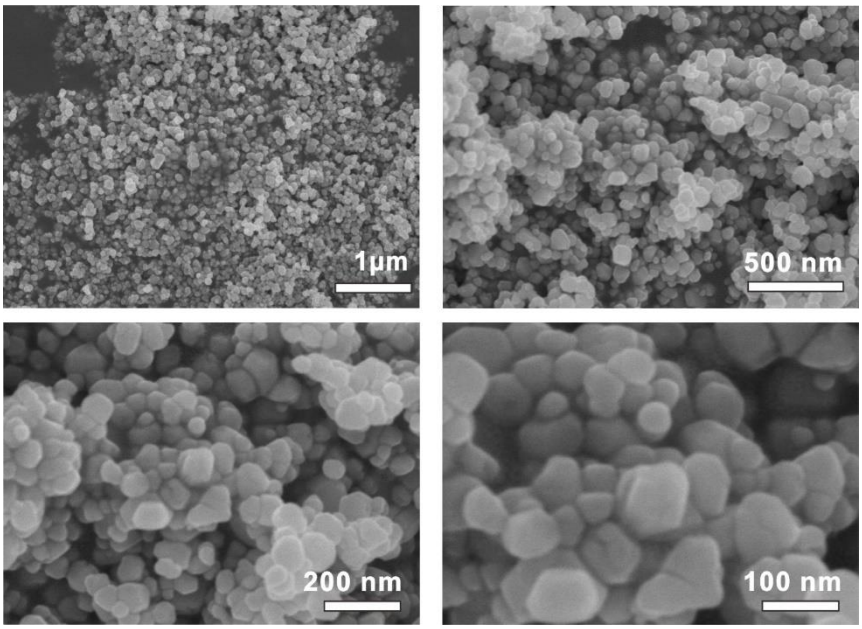

Figure S3 Mophology characterization (Related to Figure 2). SEM images of $Zn_{0.6}Cd_{0.4}S$ with different resolutions.

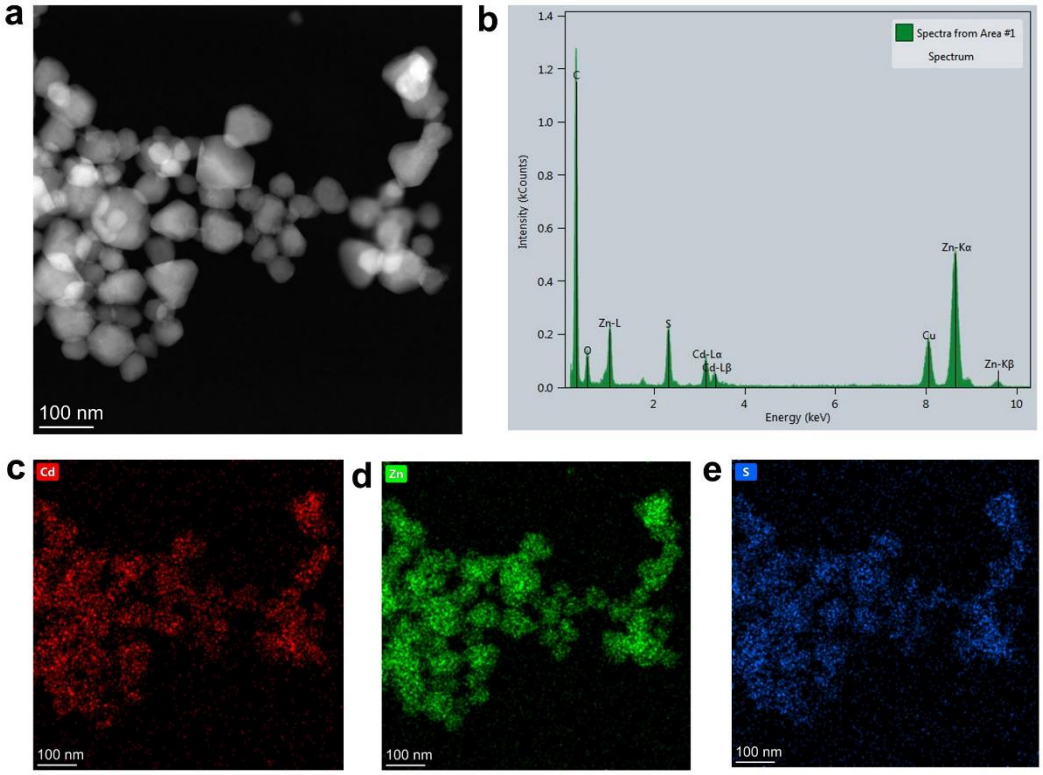

Figure S4 Mophology characterization (Related to Figure 2). (a) HAADF-STEM image at low magnification, (b) EDS spectrum of the whole area in (a), (c-e) EDS elemental maps: Cd (red), Zn (green) and S (blue) for $Zn_{0.6}Cd_{0.4}S$.

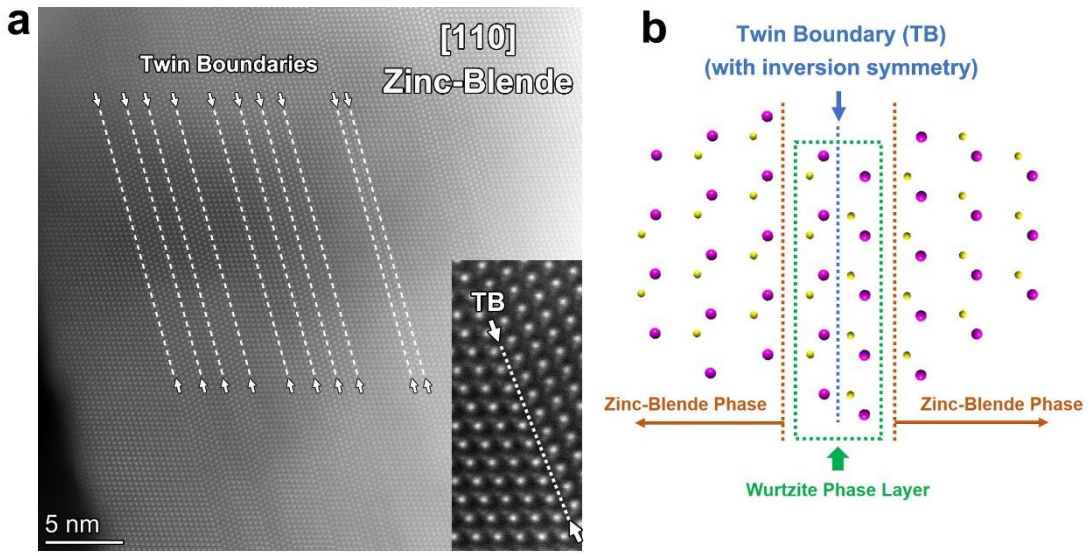

Figure S5 Structural characterization and schematic illustration of homojunction (Related to Figure 2). (a) HR-HAADF-STEM image of a zinc-blende particle and corresponding enlarged HAADF-STEM image of a twin boundary, (b) the model of twin boundary with inversion symmetry.

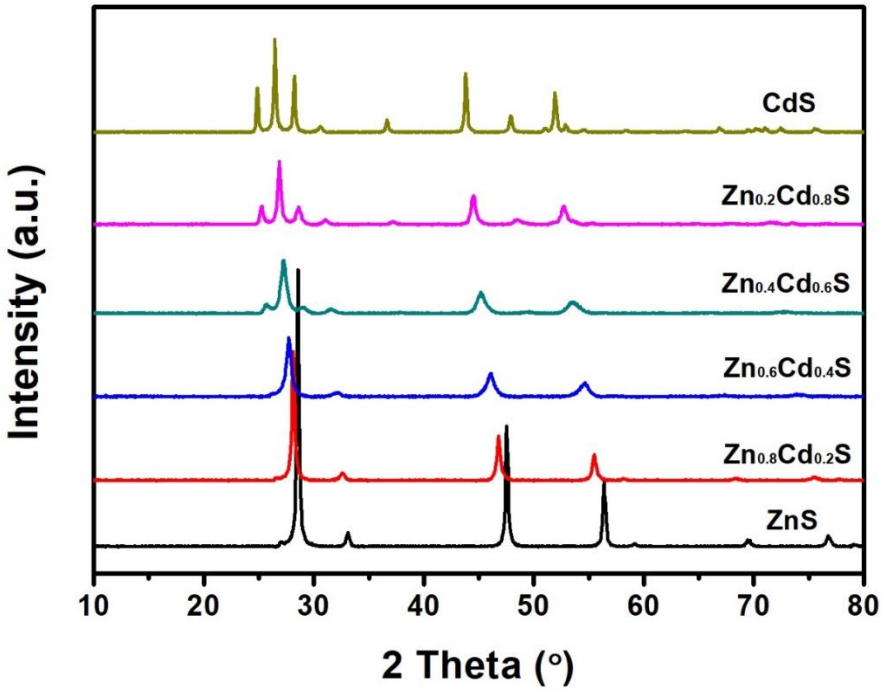

Figure S6 Crystal structure characterization (Related to Figure 2). XRD patterns of $Zn_{1-x}Cd_xS$ solid solutions.

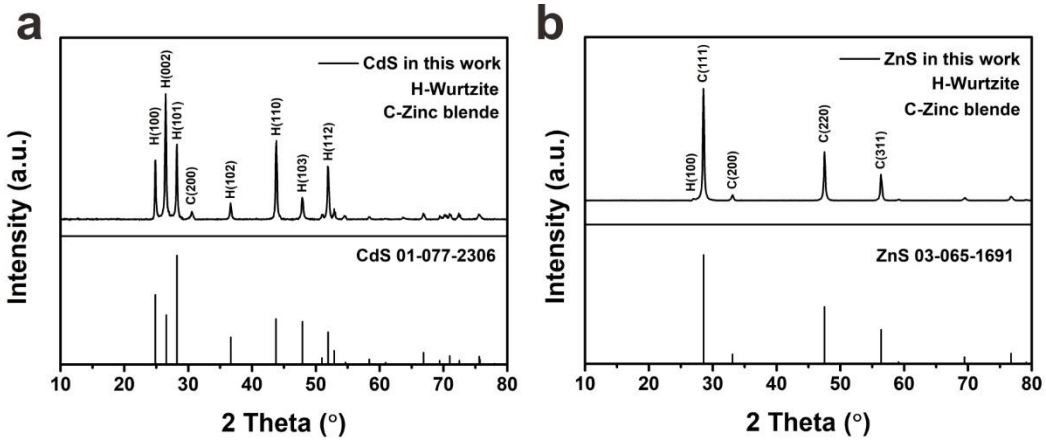

Figure S7 Crystal structure characterization (Related to Figure 2). XRD and standard patterns from JCPDS Card for CdS and ZnS.

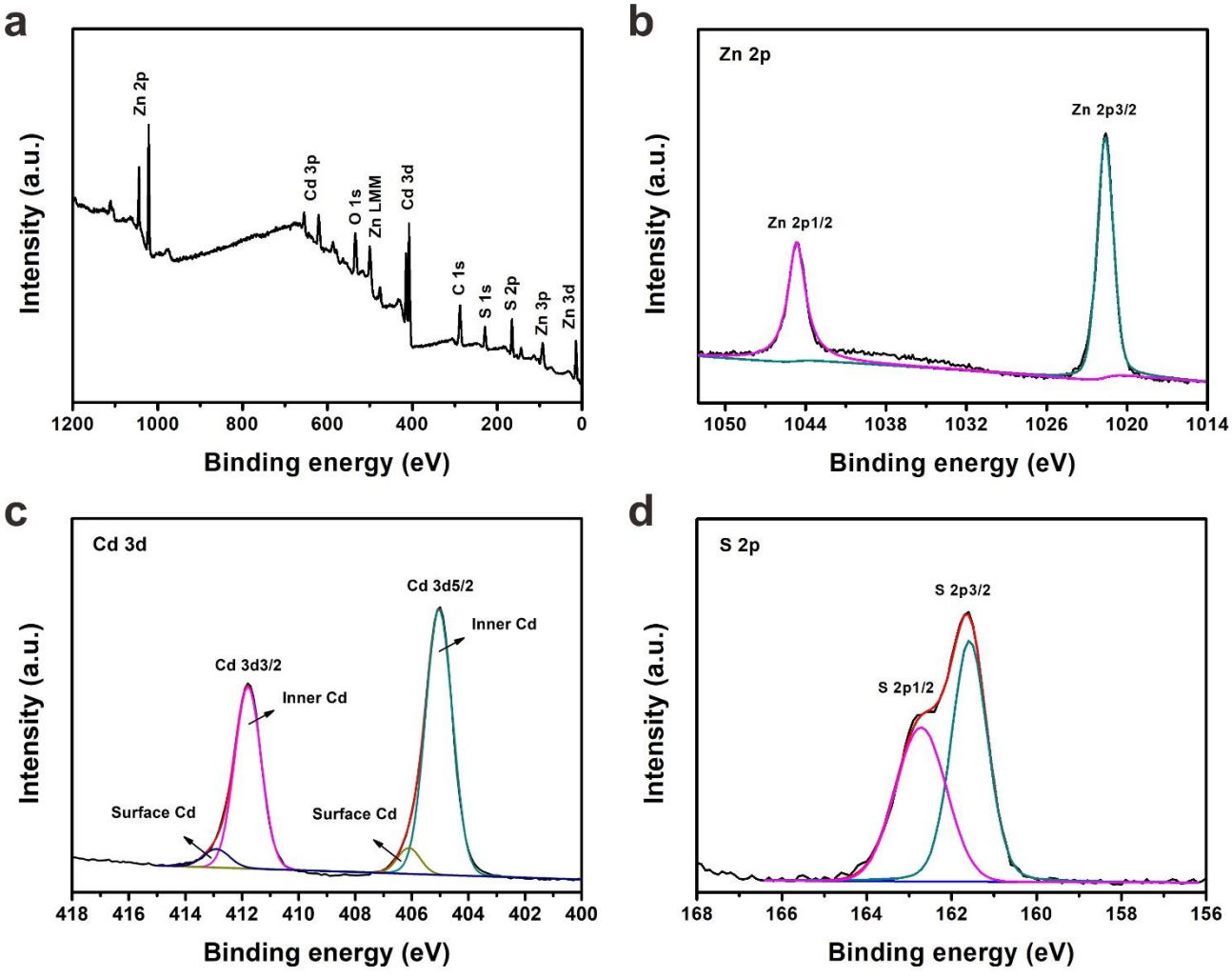

Figure S8 Component and chemical states (Related to Figure 2). (a) XPS survey spectrum and (b) Zn 2p, (c) Cd 3d and (d) S 2p spectra of $Zn_{0.6}Cd_{0.4}S$.

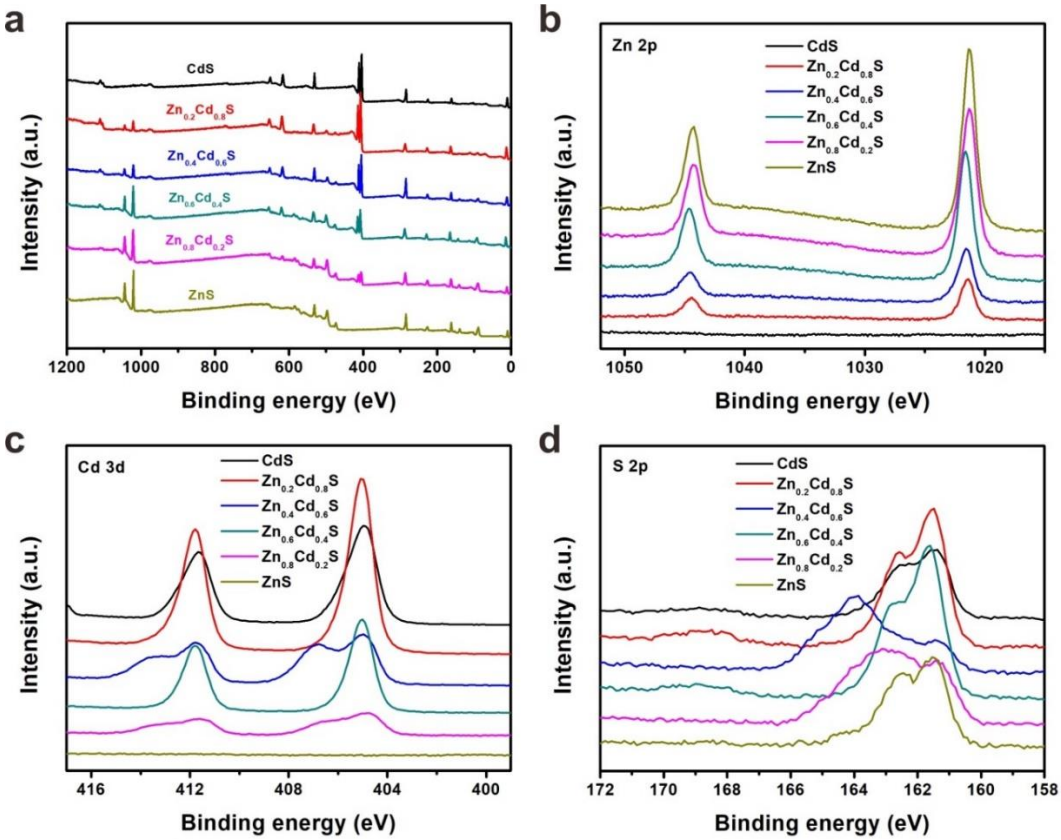

Figure S9 Component and chemical states (Related to Figure 2). (a) XPS survey spectra and high-resolution XPS spectra of (b) Zn 2p, (c) Cd 3d and (d) S 2p for $Zn_{1-x}Cd_xS$ solid solutions with different x values.

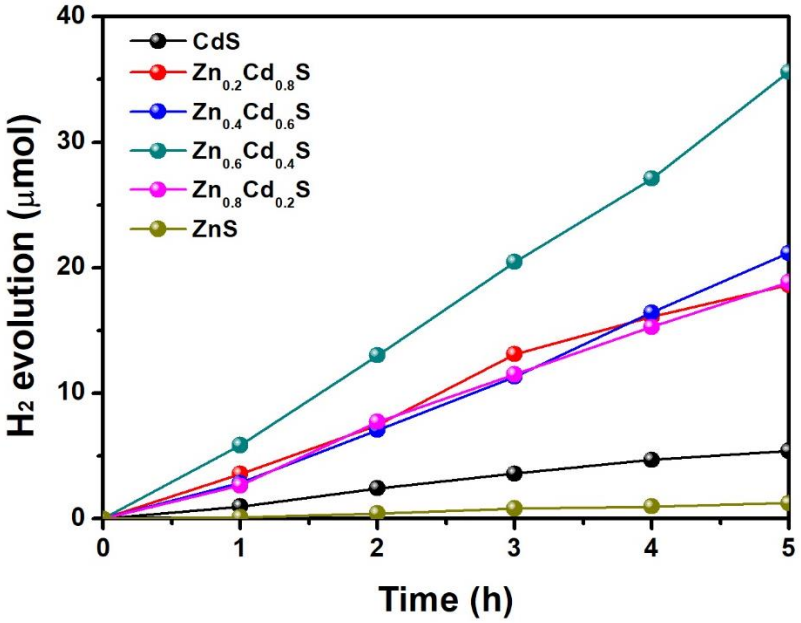

Figure S10 Hydrogen production (Related to Figure 3). (a) Photocatalytic hydrogen evolution activities of $Zn_{1-x}Cd_xS$ solid solutions in 20 g/L glucose solution.

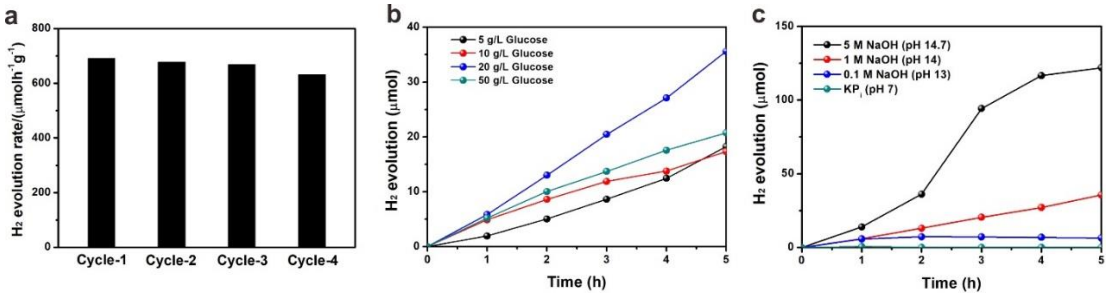

Figure S11 Hydrogen production (Related to Figure 3). (a) Photocatalytic stability of $Zn_{0.6}Cd_{0.4}S$ in four cycles and each cycle is 5 h. (b) Photocatalytic hydrogen performance of $Zn_{0.6}Cd_{0.4}S$ in different glucose concentrations. (c) Photocatalytic hydrogen performance of $Zn_{0.6}Cd_{0.4}S$ in different alkali concentration (pH).

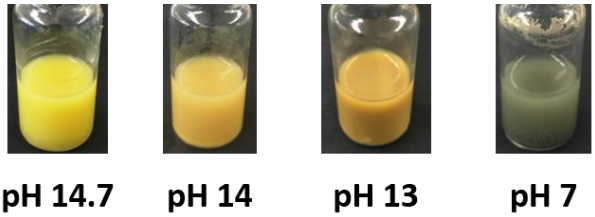

Figure S12 Photocorrosion (Related to Figure 3). Photographs of the solutions after reaction in different alkali concentration.

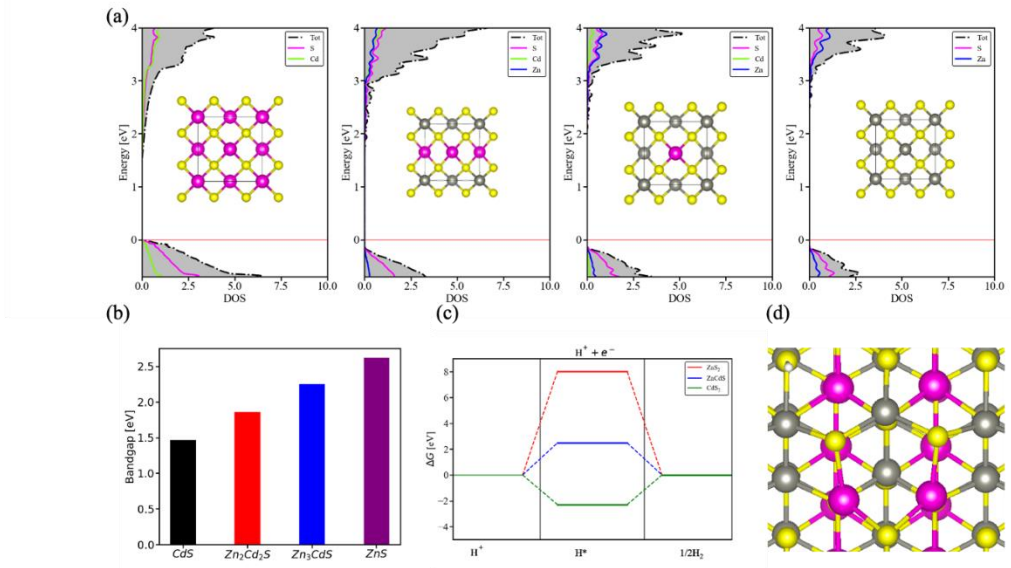

Figure S13 Structural simulation and bandgap calculation (Related to Figure 3). (a) The density of states for CdS, $Zn_{0.5}Cd_{0.5}S$, $Zn_{0.75}CdS$, ZnS (b) the band gaps for (c) The calculated = free-energy diagram of HER at the equilibrium potential for CdS, $Zn_{0.5}Cd_{0.5}S$, and ZnS. (d) The lowest energy model structure of H absorbed on $Zn_{0.5}Cd_{0.5}S$.

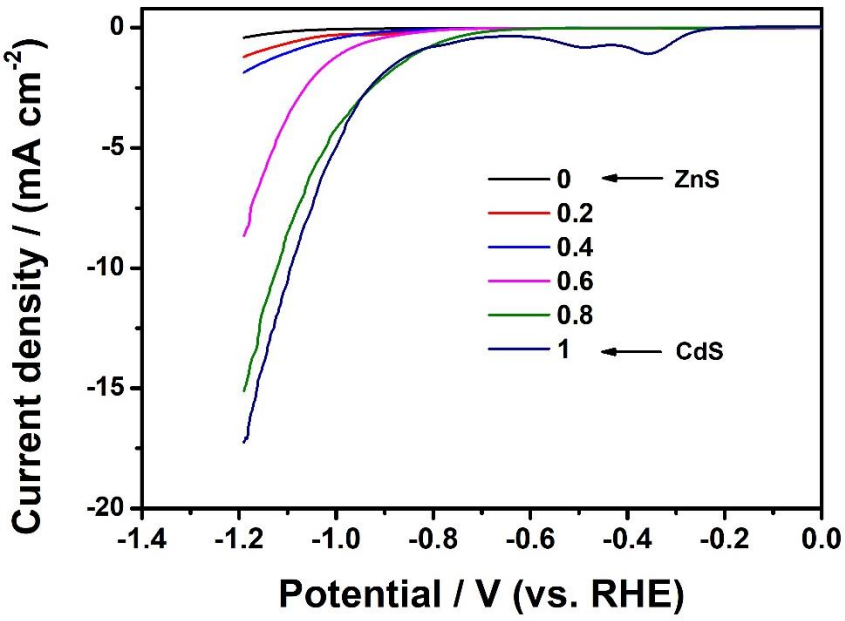

Figure S14 Electrochemical test (Related to Figure 3). Polarization curves of $Zn_{1-x}Cd_xS$ solid solutions with different x values. Condition: Pt/C with catalyst as the working electrode, Pt wire as the counter electrode and Ag/AgCl as the reference electrode, 1.0 M KOH as electrolyte. The working electrode was obtained by dip-coating 40 μL photocatalyst slurry (20 mg sample and 50 μL of 5 wt % Nafion solution were dispersed in 1 mL of 3:1 v/v water/isopropanol mixed solvent) onto the prewashed Pt/C electrode.

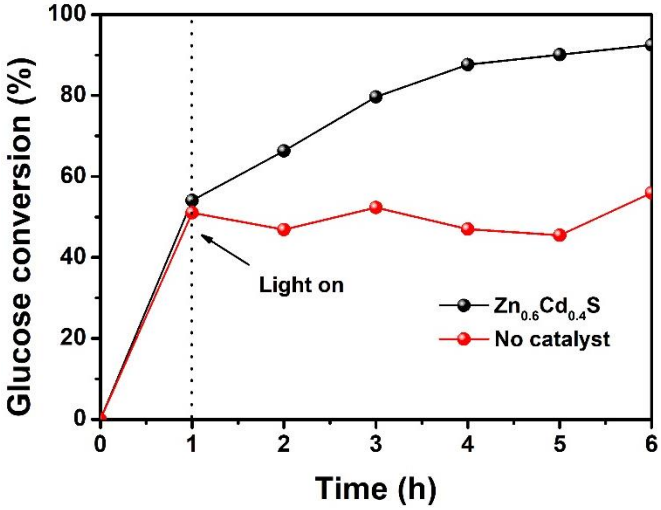

Figure S15 Glucose conversion (Related to Figure 4). Glucose conversion along with reaction time with and without photocatalyst. Reaction conditions: 10 mg photocatalyst, 5 mL 20 g/L glucose in 1 M NaOH, vacuum condition, Xenon lamp (λ = 400-780 nm), room temperature.

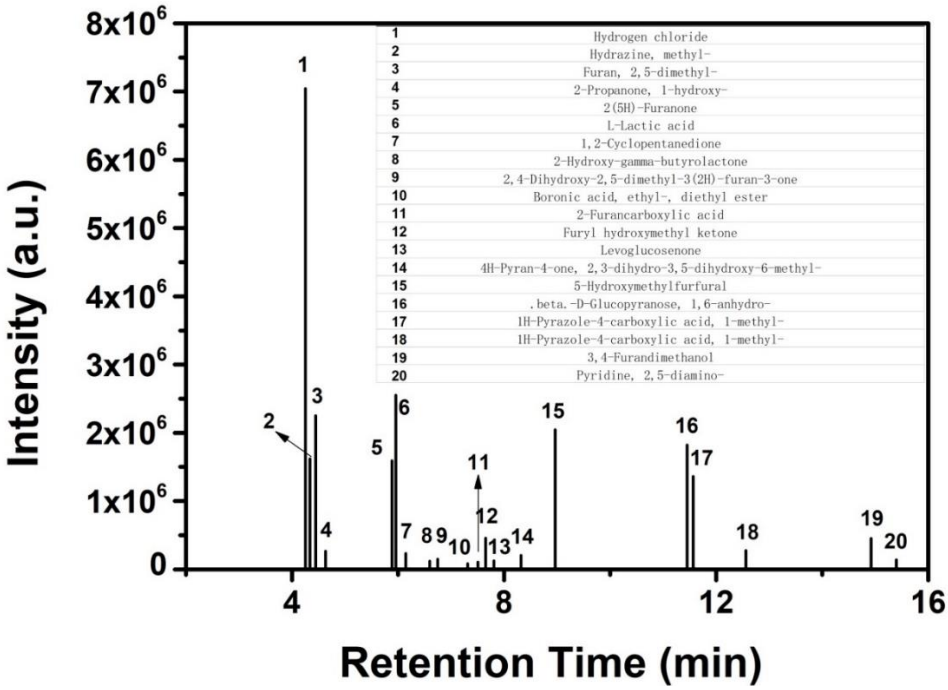

Figure S16 Products analysis (Related to Figure 4). GC-MS signals for the products in liquid after photocatalytic reaction and the matched products according to the database.

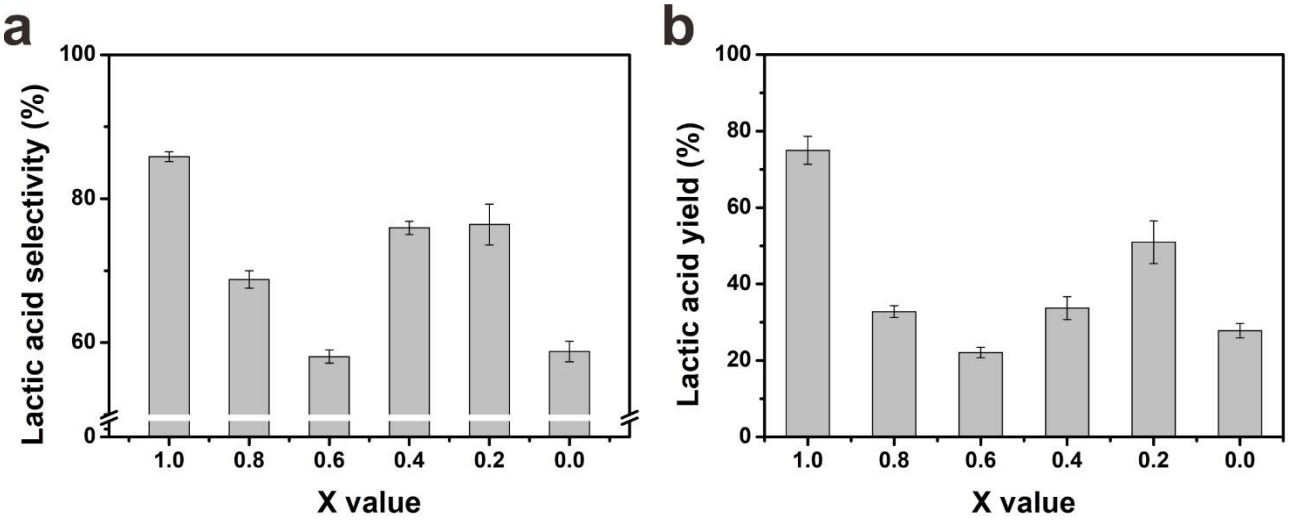

Figure S17 Lactic acid production (Related to Figure 4). Lactic acid selectivity and yield of $Zn_{1-x}Cd_xS$ solid solutions with different x values.

The glucose conversion, selectivity and yield of lactic acid were calculated using the following formulas:

Glucose conversion (%) = $((Glucose)_{in}-(Glucose)_{out})/ (Glucose)_{in}$

Lactic acid selectivity (%) = $(Lactic\ acid)_{out}/((Lactic\ acid)_{out} + (Formic\ acid)_{out} + (Fructose)_{out})$

Lactic acid yield (%) = Carbon of lactic acid / Carbon of converted glucose

Selectivity and yield values were calculated on a molar basis.

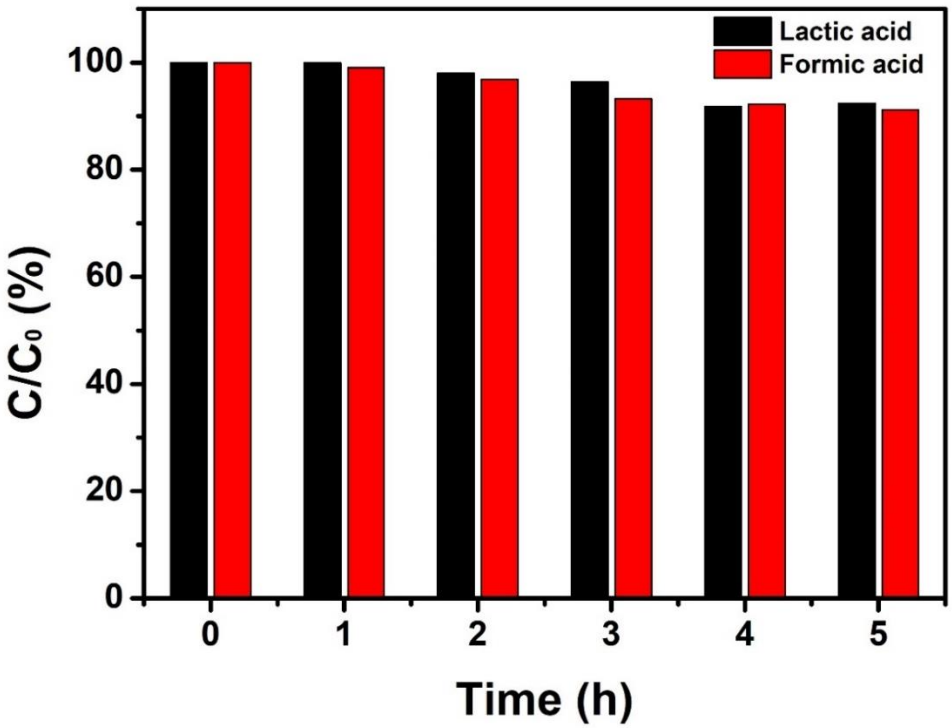

Figure S18 Stability of lactic acid and formic acid during the reaction (Related to Figure 4). Lactic acid and formic acid conversion over $Zn_{0.6}Cd_{0.4}S$. Reaction conditions: 10 mg photocatalyst, 5 mL 20 g/L lactic acid or formic acid in 1 M NaOH, vacuum condition, Xenon lamp (λ = 400-780 nm), room temperature.

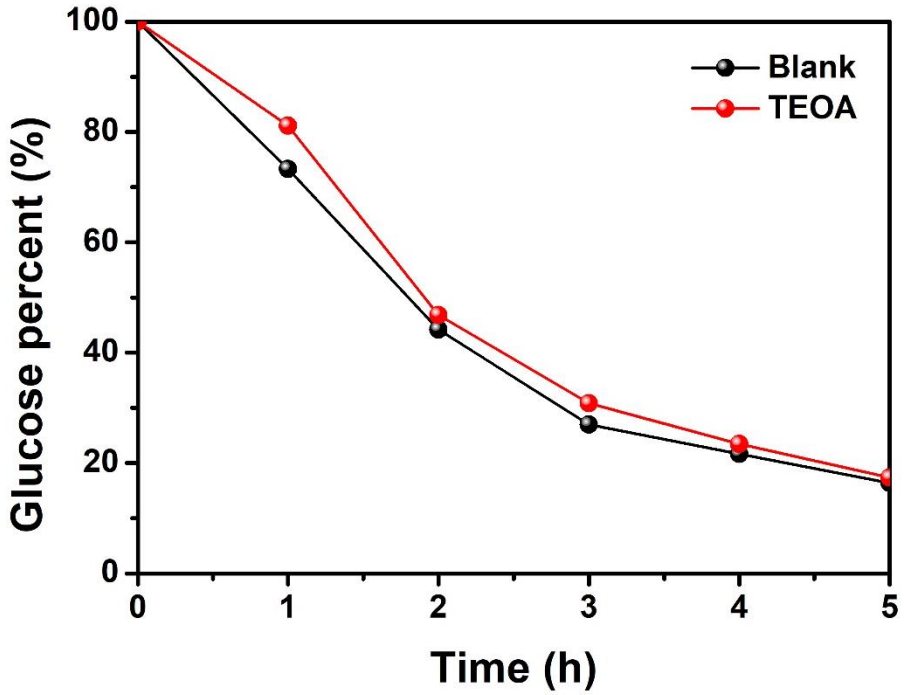

Figure S19 Scavenger test (Related to Figure 5). Glucose conversions without any sacrificial agent and in presence of TEOA over $Zn_{0.6}Cd_{0.4}S$.

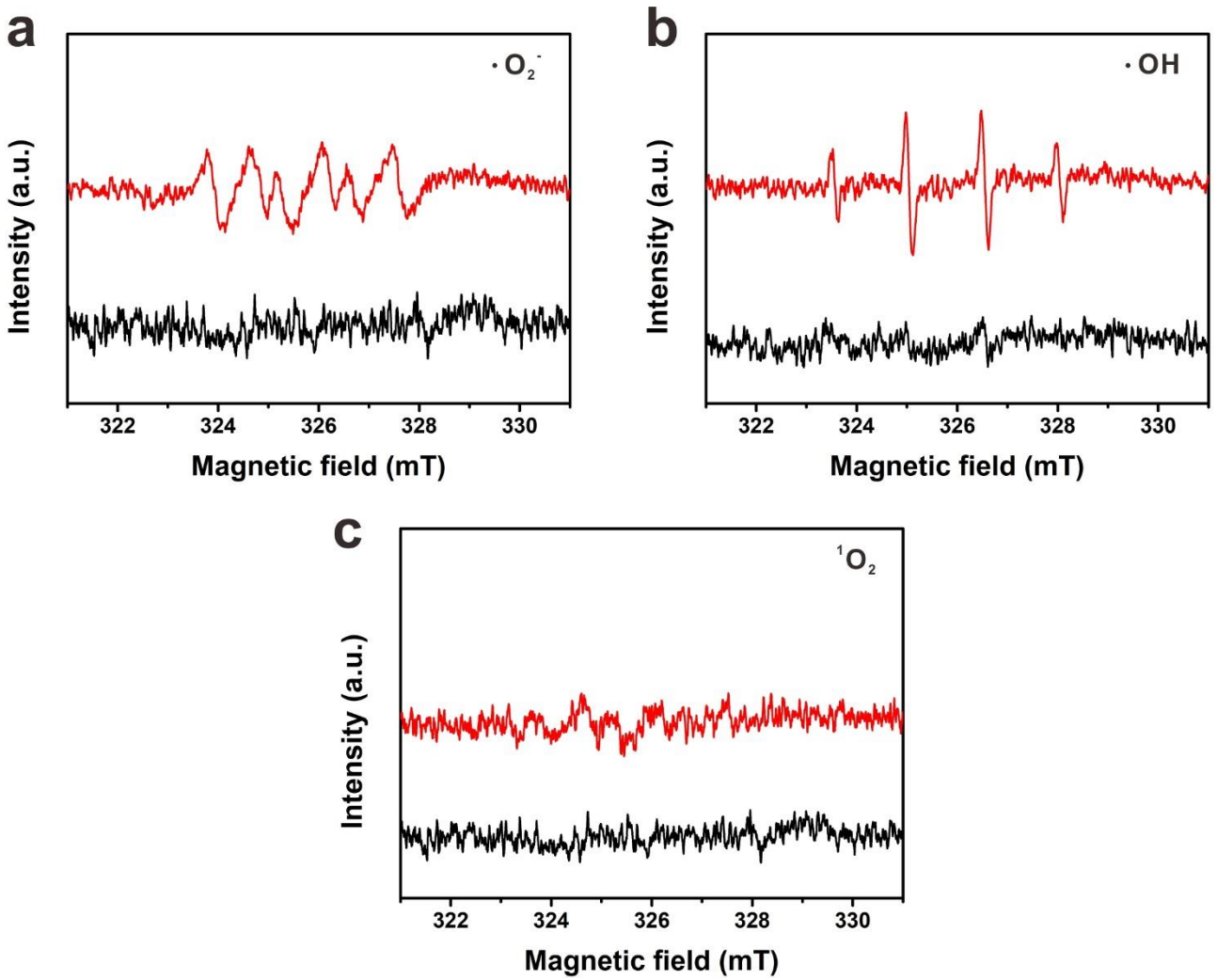

Figure S20 Active oxygen species (Related to Figure 5). DMPO ESR spin-trapping for (a) $\cdot O_2^-$ and (b) ·OH, TEMPONE ESR spin-trapping for (c) $^1O_2$ over $Zn_{0.6}Cd_{0.4}S$ (black line: under dark condition and red line: with light irradiation).

Transparent Methods

Materials

All the reagents in this experiment were of analytical grade and commercially available. Zinc acetate dihydrate ($Zn(CH_3COO)_2 \cdot 2H_2O$, 98.0%), cadmium acetate dihydrate ($Cd(CH_3COO)_2 \cdot 2H_2O$, 98.0%), thioacetamide (TAA, 99.0%), 1-octanol (99.0%), ethylene glycol (EG, 99.8%) and ethanol were purchased from Millipore Sigma.

Synthesis of $Zn_{1-x}Cd_xS$ solid solution

In typical, 8 mmol TAA was dissolved in a mixed solution containing 20 mL EG, 10 mL 1-octanol and 10 mL water. Then, a total 4 mmol of $Zn(CH_3COO)_2 \cdot 2H_2O$ and $Cd(CH_3COO)_2 \cdot 2H_2O$ with the desired atomic ratio was added into the above solution. The obtained aqueous solution was transferred to a 50 mL Teflon-lined stainless-steel autoclave after 30 min of continuous stirring and heated at 180 ℃ for 4 h. The resulting precipitate was collected after centrifugation, washed with ethanol three times and dried in an oven at 80 ℃ overnight. A series of $Zn_{1-x}Cd_xS$ solid solutions with x values of 0, 0.2, 0.4, 0.6, 8 and 1 can be prepared by changing the molar ratio between $Zn(CH_3COO)_2 \cdot 2H_2O$ and $Cd(CH_3COO)_2 \cdot 2H_2O$.

Characterization

The crystalline phase in the samples was examined by powder X-ray diffraction (XRD, D8 ADVANCE) equipped with a Cu anode X-ray tube (Cu Kα X-rays, λ=1.54056 Å). The rough surface morphology of the samples was observed with a field-emission scanning electron microscope (SEM, Hitachi S-4800). The local structure of the materials has been determined using a double aberration corrected transmission electron microscope (TEM, Thermo Fisher Titan Themis) equipped with a Super-X energy dispersive X-ray detector (EDX) at 300 keV. X-ray photoelectron spectroscopy (XPS) to determine the surface chemical composition and binding energy of constituting elements were recorded on a customized X-ray photoelectron spectrometer (Kratos AXIS Ultra DLD equipped with a monochromatic Al Kα source). All the raw data was calibrated using the C (1s) peak of adventitious carbons at a binding energy 284.8 eV. The UV-vis absorption spectra were recorded in a diffuse reflectance mode on a SHIMADZU UV-Vis spectrophotometer with an integrating sphere scanning in a spectral range of 300-800 nm. The Brunauer-Emmett-Teller (BET) specific surface areas of the powders were determined using N_2 adsorption-desorption isotherms at 77 K on a Gemini

VII (Micromeritics Corp.). The zeta potential was measured using the Nanoplus zeta analyzer (Nano-ZS, Malvern).

Photocatalytic glucose conversion

Typically, the photocatalytic testing was performed in closed glass vials (12 mL) at room temperature using a 300 W Xenon lamp (Excelitas Tech.). 10 mg photocatalyst was dispersed in a mixed solution of 20 g/L substrate and 5 mL NaOH (1 M) solution. The closed glass vial containing the above mixture was sonicated and degassed for 0.5 h and finally irradiated under AM1.5 G solar simulated light. The evolved H_2 was periodically quantified by using gas chromatography (GC, PerkinElmer Clarus 590) equipped with a Molecular Sieve 5A packed column and a thermal conductivity detector (TCD). The glucose stock solutions (for calibration) and reaction products were analyzed by using a 1200 HPLC Agilent system equipped with a refractive index detector (RID) and a photodiode array detector (DAD). The column was Hi-Plex H (6.5 × 300 mm, 8 μm, Agilent) and 0.005 M H_2SO_4 was used as an eluting solvent with a flow rate of 0.5 mL/min. Each experiment was repeated for three time to have the error bar.